AD A042561

RADC-TR-77-155
Final Technical Report
April 1977

12 NW

IR WINDOW STUDIES

Electronic Sciences Laboratory
University of Southern California
Los Angeles, California 90007

DDC
AUG 9 1977
C

Approved for Public Release;
Distribution Unlimited.

Sponsored by
Defense Advanced Research Projects Agency
ARPA Order 2055

ROME AIR DEVELOPMENT CENTER
AIR FORCE SYSTEMS COMMAND
GRIFFISS AIR FORCE BASE, NEW YORK 13441

AD No.
DDC FILE COPY

ARPA Order No. 2055

Program Code No. 3D10

Effective Date of Contract:
1 September 1975

Contractor:
University of Southern California

Contract No. F19628-76-C-0162

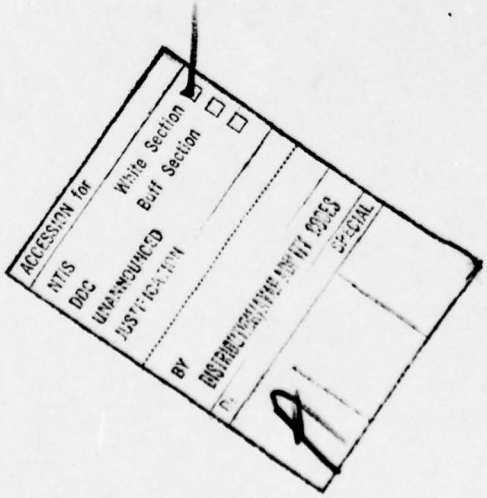
Principal Investigator and Phone No:
Prof. John H. Marburger
(213) 746-2351

RADC/ETSS Project Scientist and Phone No.:
Alfred Kahan (617) 861-4014

Contract Expiration Date:
30 September 1976

The views and conclusions contained in this document are those of the authors and should not be interpreted as necessarily representing the official policies, either expressed or implied, of the Defense Advanced Research Projects Agency or the U.S. Government.

Qualified requestors may obtain additional copies from the Defense Documentation Center. All others should apply to the National Technical Information Service.



UNCLASSIFIED

SECURITY CLASSIFICATION OF THIS PAGE (When Data Entered)

(19) REPORT DOCUMENTATION PAGE

READ INSTRUCTIONS BEFORE COMPLETING FORM

(18) 1. REPORT NUMBER: RADC-TR-77-155

2. GOVT ACCESSION NO.

3. RECIPIENT'S CATALOG NUMBER

(6) 4. TITLE (and Subtitle): IR WINDOW STUDIES,

(9) 5. TYPE OF REPORT & PERIOD COVERED: Final Report. 1 Sep 75 — 1 Sep 76

6. PERFORMING ORG. REPORT NUMBER

(10) 7. AUTHOR(s): J. H. Marburger, Michael Bass

(15) 8. CONTRACT OR GRANT NUMBER(s): F19628-76-C-0162, ARPA Order-2055

9. PERFORMING ORGANIZATION NAME AND ADDRESS
University of Southern California
Electronic Sciences Laboratory
Los Angeles, California 90007

10. PROGRAM ELEMENT, PROJECT, TASK AREA & WORK UNIT NUMBERS
PE: 61101E
Proj: 562108-09

11. CONTROLLING OFFICE NAME AND ADDRESS
Defense Advanced Rsch Projects Agency
1400 Wilson Boulevard
Arlington, VA 22209

(11) 12. REPORT DATE: April 1977

13. NUMBER OF PAGES: 101

14. MONITORING AGENCY NAME & ADDRESS (if different from Controlling Office)
Deputy for Electronic Technology (RADC)
Hanscom AFB, Massachusetts 01773
Monitor/ Alfred Kahan/ ETSS

15. SECURITY CLASS. (of this report): UNCLASSFIED

15a. DECLASSIFICATION/DOWNGRADING SCHEDULE

16. DISTRIBUTION STATEMENT (of this Report)

Approved for public release; distribution unlimited

(12) 191 p.

17. DISTRIBUTION STATEMENT (of the abstract entered in Block 20, if different from Report)

18. SUPPLEMENTARY NOTES

This research was sponsored by Defense Advanced Research Projects Agency ARPA Order No. 2055

19. KEY WORDS (Continue on reverse side if necessary and identify by block number)

Defects in ZnSe; 10.6 μm pulsed laser damage; Alkali-halides; Thin films; 3.8 μm pulsed laser damage; Sapphire; Alkaline-earth-fluorides; Thermal lensing; Strain optic coefficients; Stress induced birefringence

20. ABSTRACT (Continue on reverse side if necessary and identify by block number)

Research concerned with several aspects of the infrared laser window problem is described. Measurements of the Hall effect and electrical conductivity were used to study defects in ZnSe and it was found that a defect model governed by ionic defects can be developed.

Pulsed laser damage studies revealed that there are still significant sample to sample variations even in today's so-called improved materials.

DD FORM 1 JAN 73 1473 EDITION OF 1 NOV 65 IS OBSOLETE
S/N 0102-014-6601

361620

UNCLASSIFIED

SECURITY CLASSIFICATION OF THIS PAGE (When Data Entered)

Alkali-halides which damage at 5-10 GW/cm^2 can be obtained but surface damage to conventionally polished samples occurs at ~1/10 of the bulk threshold. Damage to 10.6 μm anti-reflection coatings is dominated by defects and in general occurs at ~0.4 GW/cm^2. Sapphire has a high 3.8 μm laser damage threshold (~25 GW/cm^2) and so, because of its mechanical properties, should be considered for use in HF/DF laser optics.

Thermal lensing, strain optic coefficients and the dependence of stress induced birefringence on crystal orientation were studied. In general, acceptable agreement between theory and experiment was found. There is theoretical reason to believe that it is possible to design a polycrystal which has significantly less thermal stress induced birefringence than a single crystal.

SUMMARY

Research concerned with several aspects of the infrared laser window problem is described. Measurements of the Hall effect and electrical conductivity were used to study defects in ZnSe and it was found that a defect model governed by ionic defects can be developed.

Pulsed laser damage studies revealed that there are still significant sample to sample variations even in today's so-called improved materials. Alkali-halides which damage at 5-10 GW/cm^2 can be obtained but surface damage to conventionally polished samples occurs at ~1/10 of the bulk threshold. Damage to 10.6 μm anti-reflection coatings is dominated by defects and in general occurs at ~0.4 GW/cm^2. Sapphire has a high 3.8 μm laser damage threshold (~25 GW/cm^2) and so, because of its mechanical properties, should be considered for use in HF/DF laser optics.

Thermal lensing, strain optic coefficients and the dependence of stress induced birefringence on crystal orientation were studied. In general, acceptable agreement between theory and experiment was found. There is theoretical reason to believe that it is possible to design a polycrystal which has significantly less thermal stress induced birefringence than a single crystal.

PREFACE

Responsibility for the research conducted in this program was divided in the following manner:

Dr. J. Marburger	Principal Investigator, theoretical analyses
Dr. M. Bass	Pulsed Laser Damage Studies
Dr. W.H. Steier	Stress Induced Birefringence
Dr. F.A. Kroger	Defect Chemistry in ZnSe
Dr. H. Narayanan	Defect Structure in ZnSe
Dr. W.G. Spitzer	Absorption Studies of CdTe and ZnSe

Dr. K.M. Leung and Mr. C. Tang from USC and Mr. M.J. Soileau of the Naval Weapons Center participated in the laser damage measurements. The Hughes Research Laboratory provided coatings and samples of RAP grown alkali-halides for these studies. Mr. R. Joiner and Dr. C.P. Christensen participated in the measurements of stress-induced birefringence and M. Flannery worked on the theory. Mr. A. Ray worked on the studies of defect chemistry in ZnSe and Dr. B.V. Dutt participated in the absorption studies.

TABLE OF CONTENTS

		Page
REPORT DOCUMENTATION PAGE DD FORM 1473		i
SUMMARY		iii
PREFACE		iv
TABLE OF CONTENTS		v
LIST OF ILLUSTRATIONS		vi
LIST OF TABLES		x
I.	INTRODUCTION	1
II.	DEFECTS IN ZnSe	3
	A. Defect Chemistry of ZnSe	3
	1. ZnSe:Al	3
	2. ZnSe:As	4
	3. ZnSe:Ga	5
	B. An Electron Microscope Investigation of Structural Imperfections in II-VI Compounds (ZnSe and CdTe)	6
	1. Lattice Defects in Ga-doped ZnSe	9
	C. Absorption Studies of CdTe and ZnSe	14
III.	PULSED LASER INDUCED DAMAGE	
	A. Re-examination of Laser Induced Breakdown in the Alkali-Halides at 10.6 μm	16
	1. Introduction	16
	2. Experimental	16
	3. Comparison of N on 1 and 1 on 1 Damage Thresholds	18
	4. Comparison of Materials	19
	5. Dependence of Damage Thresholds for Different Spot Sizes	21
	B. Pulse Laser Damage in Three Layer 10.6 μm AR Coatings on KCl	22
	1. Introduction	22
	2. Experimental	22
	3. Results	24

TABLE OF CONTENTS (continued) Page

C. Pulsed Laser Induced Damage at the DF Laser Wavelength 29

1. Introduction 29

2. Experimental 29

3. Damage in the 2-5 μm Optical Materials 34

4. Results of Damage Threshold Measurements 40

D. Summary of Pulsed Laser Damage Thresholds for Infrared Windows and Coatings 42

E. CW Damage to Optical Coatings - Comparison with Pulse Damage Thresholds 45

F. Data Acquisition System and Survival Curve Technique for Identifying Pulse Laser Damage Mechanisms 48

IV. NON-CATASTROPHIC OPTICS DEGRADATION

A. Thermal Lensing 51

B. Strain-optic Coefficient Measurements 51

C. Strong Variations in Stress-Induced Birefringence in BaF_2 Due to Crystal Orientation 51

D. Theory of Thermally Induced Birefringence in Polycrystalline Media 57

V. CONCLUSIONS

A. Defects in ZnSe 59

B. Pulsed Laser Induced Damage 60

C. Non-Catastrophic Optics Failure 61

VI. RECOMMENDATIONS 62

REFERENCES 63

BIBLIOGRAPHY 65

APPENDIX A: Vibrational Modes of Defects in $Zn_xCd_{1-x}Te:P$ and $Mg_xCd_{1-x}Te:P$

APPENDIX B: Free Carrier Absorption of n-Type ZnSe:Al

LIST OF ILLUSTRATIONS

Page

1. (a) A brightfield micrograph showing surface contaminants on a ZnSe thin foil specimen prepared by using the HCl-H_2O_2-H_2O chemical polishing solution. Note the moire' fringes associated with the surface contaminants..... 8

   (b) Selected area electron diffraction from a heavily contaminated specimen showing diffuse rings resulting from the contaminant superimposed on the spot pattern from ZnSe.. 8

2. Brightfield micrograph showing extrinsic stacking fault in the as-grown ZnSe doped with Ga..... 10

3. Brightfield micrograph of a Ga-doped ZnSe annealed at 700°C under a Zn-partial pressure of 10^{-3} atoms. Arrows show isolated precipitates..... 10

4. Brightfield micrograph showing the presence of prismatic dislocation loops in a Ga-doped ZnSe sample annealed at 700°C under a Zn-partial pressure of 3×10^{-3} atms..... 12

5. (a) Brightfield micrograph showing the distribution of vacancy type prismatic loops in Ga-doped ZnSe following a 700°C anneal under a Zn partial pressure of 3×10^{-2} atms..... 12

   (b) Brightfield micrograph showing the initial stages of formation of a dislocation helix (arrow) in the same sample as that in Fig. 5(a)..... 13

   (c) Brightfield micrograph showing a fully transformed helix in the same sample as above..... 13

   (d) Brightfield micrograph showing dislocation tangles associated with unidentified precipitates (arrow) in the sample annealed at 700°C under a $P_{Zn} = 3 \times 10^{-2}$ atms..... 13

6. Brightfield dislocation showing the presence of precipitates and decorated dislocations (arrow) in a Ga-doped ZnSe annealed at 700°C under a Zn-partial pressure of 0.1 atm..... 15

7. Micrograph of ZnSe/ThF_4/ZnSe coating on KCl showing crazing caused by thermal cycling. The spot in the photo is a pulsed laser induced damage site produced on the coating after the crazing occurred..... 26

LIST OF ILLUSTRATIONS (continued) Page

8. Laser damage to a ZnSe/KCl/ZnSe on KCl A-R coating showing the role of defects (probably absorbing inclusions) in the damage process..... 28

9. Temporal profile of a multi-line DF laser pulse. The dashed curve represents the equivalent pulse constructed in order to deduce a damage threshold intensity..... 30

10. Typical oscilloscope traces for bulk damage in SrF_2 due to DF laser light. The upper trace is the incident pulse waveform and the lower trace is the transmitted pulse waveform. When damage occurs the transmitted pulse waveform is attenuated... 32

11. Nomarski micrographs of exit surface damage to SrF_2. The lower photograph is an enlargement of the central region of the irradiated site showing interference ripples..... 35

12. Nomarski micrographs of entrance surface damage to CaF_2. The lower photograph is an enlargement of the damage site showing the aligned cracks..... 36

13. Nomarski micrographs of entrance surface damage to the same CaF_2 crystal as in figure 12. The enlarged picture shows clearly the edge of a twin plane which divides two sets of aligned cracks..... 37

14. Nomarski micrographs of entrance surface damage to a MgG_2 single crystal. No aligned cracks are observed in this case since MgF_2 has no well defined cleavage planes..... 38

15. Comparison of bright field and phase contrast illumination micrographs. Crazing is present as well as defects which are not obvious in bright field illumination..... 46

16. Pulsed and CW 10.6 μm laser damage to a $ZnSe/ThF_4/ZnSe$ anti-reflection coating on KCl..... 47

17. Operation of the CdTe pulse modulator. Upper photo shows the input laser waveform. Lower photo shows the modulated waveform..... 49

18. Oscilloscope photograph of transmitted (upper trace) and input (lower trace) pulse waveforms required for survival curve analysis of pulse laser damage mechanisms. Sample was ZnSe 50

LIST OF ILLUSTRATIONS (continued) Page

19. Schematic of experiment..... 52

20. Transmission pattern of cross polarization - normal incidence (⟨111⟩) 53

21. Transmission pattern of cross polarization - large angle incidence 53

22. Euler angles describing tilt and rotations of BaF_2 sample..... 55

LIST OF TABLES

		Page
I.	Summary of Experimental Parameters	17
II.	Comparison of N on 1 and 1 on 1 Laser Damage Thresholds	19
III.	Relative Breakdown Fields at 10.6 μm - Normalized to E_{NaCl}	20
IV.	Comparison of Damage Thresholds for Different Spot Sizes	21
V.	(List of symbols)	24
VI.	Results of Laser Damage Tests	27
VII.	Summary of Experimental Parameters	31
VIII.	Determination of Focal Spot Diameter for DF Laser and 3.58 cm Focal Length Lens	33
IX.	Some Properties of Potentially Useful 2-5 μm Materials	39
X.	Scattering in 2-5 μm Window Materials ($x10^3$)	41
XI.	Threshold for Bulk Laser Irradiation Induced Damage	40
XII.	Composite Summary of Pulse Laser Damage Thresholds in the Infrared	42
XIII.	Pulse Laser Induced Damage Thresholds at 10.6 μm for IR Window Materials	43
XIV.	Pulse Laser Induced Damage Thresholds at 3.8 μm (DF laser) for IR Window Materials	44
XI.	Pulse Laser Damage Threshold at 10.6 μm for Optical Coatings	44

I. INTRODUCTION

This report describes several research activities related to the problem of infrared windows for high power laser systems. The properties of various defects in ZnSe were studied by means of Hall effect and electrical conductivity measurements and by electron microscopy techniques. It was found that donor (Al) doped material showed electron concentrations which were proportional to the square root of the zinc pressure and the donor concentration. Acceptor (As) doped material showed electron concentrations inversely proportional to the acceptor concentration. Through a combination of the present results with those of other workers a defect model can be developed which is governed by ionic defects due to ionized dopants and native defects.

Annealing Ga-doped ZnSe under various Zn partial pressures was found to induce noticeable changes in the defect substructure. At moderate Zn pressures the microstructure revealed the formation of a high density of unfaulted prismatic loops. These have been identified to be caused by the condensation of excess Zn and also by Se vacancies. At still higher Zn pressures, the loop concentration decreased drastically and only some, as yet, unidentified precipitate was found.

Pulsed laser damage studies were conducted at 10.6 μm on infrared transmissive materials and anti-reflection coatings. The first pulsed laser damage measurements to alkaline-earth fluorides at 3.8 μm were conducted in a joint effort with the Naval Weapons Center at China Lake. Certain coatings were tested for both pulsed and CW laser damage thresholds. Pulsed laser damage thresholds were summarized and the following general statements were found possible: 1) at 10.6 μm, alkali-halides damage at ~5-10 GW/cm^2, 2) their uncoated surfaces damage at 1-2 GW/cm^2, 3) anti-reflection coatings damage at ~0.4 GW/cm^2 and 4) at 3.8 μm, alkaline-earth fluorides damage at ~20-25 GW/cm^2. These observations can be used to guide high power laser system designers.

Thermal lensing, strain optic coefficients and the dependence of stress induced birefringence on crystal orientation were studied in another part of this work. In general, acceptable agreement between theory and experiment was obtained. The experimental data obtained in the study of thermal stress induced birefringence and the theoretical analyses suggest the possibility that a polycrystal can be designed in which this effect is significantly reduced.

II. DEFECTS IN ZnSe

(F.A. Kroger, H. Narayanan, A. Ray, W.G. Spitzer, B.V. Dutt)

A. Defect Chemistry of ZnSe

Electrical behavior of Al, Ga and As in ZnSe was investigated by high temperature and room temperature electrical conductivity and Hall measurement.

A.1 ZnSe:Al

High temperature electron concentration in ZnSe:Al varied as $p_{Zn}^{1/2}[Al]^{1/2}$ at low and medium zinc pressure but at high Zn pressure, electron concentration in ZnSe doped with 3 and 30 ppm Al was independent of p_{Zn}. The first case can be explained by the incorporation reaction

$$Zn(g) + V''_{Zn} \rightarrow Zn^{x}_{Zn} + 2e'$$

or $$[e']^2 = K_{ZnV}[V''_{Zn}]\, p_{Zn} \quad .$$

For electrical neutrality

$$[Al^{\bullet}_{Zn}] = 2[V''_{Zn}] \text{ and an Al balance } [Al^{\bullet}_{Zn}] \approx [Al]_{total},$$

$$[e'] = K_{ZnV}[\tfrac{1}{2}Al]^{1/2} p_{Zn}^{1/2}$$

Independence of $[e']$ of p_{Zn} in ZnSe containing low amounts of Al at high p_{Zn} is due to $[e'] = [Al^{\bullet}_{Zn}] = [Al]_{total}$ = constant. In this range the electron concentration is essentially independent of temperature. In the Zn pressure range in which $[e'] \propto p_{Zn}$, the electron concentration

decreases with increasing temperature. The temperature dependence of the electron concentration at a particular p_{Zn} gives the activation energy of the equilibrium constant K_{ZnV}:

$$K_{ZnV} = K^{\circ}_{ZnV}{}^{1/2} \exp\left(-\frac{\Delta H_{ZnV}}{2kT}\right) \text{ with } \Delta H_{ZnV} = -1.0 \text{ eV}$$

Conductivity and electron concentration were also measured in crystals quenched to room temperature after being equilibrated at high temperature under well defined Zn pressures. At high p_{Zn} the room temperature electron concentrations were equal to those at high temperature indicating that Al forms a very shallow donor level. At room temperature, there is a cut-off in electron concentration at low p_{Zn}. For a sample with fixed Al content, the Zn pressure at which the cut-off takes place moves to higher Zn pressure with increasing annealing temperature. But for a particular annealing temperature no definite relationship was observed between cut-off p_{Zn} and Al content. The cut-off of the electron concentration is presumably due to trapping of electrons by both native defects (V_{Zn}) and impurities with deep levels, the latter present in different concentrations in the various crystals. Crystals beyond the cut-off points had a high resistance.

A.2 ZnSe:As

As is expected to act as an acceptor in ZnSe. High temperature Hall measurements under Zn vapor were carried out on single crystals ZnSe:50 ppm As. Electron concentrations were much lower than those measured for donor-doped crystals. They varied $\propto p_{Zn}^{1/2}$ and increased with increasing temperature. As shown earlier,

$$[e'] = K_{ZnV}^{1/2} [V''_{Zn}]^{1/2} p_{Zn}^{1/2}$$

Assuming Frenkel disorder on the Zn-sub lattice to be predominant,

$$[As'_{Se}] = 2[Zn_i^{\bullet\bullet}]$$

then $[V''_{Zn}] = \frac{2K_F}{[As_{Se}]}$ and $[e'] = K_{ZnV}^{1/2} K_F^{1/2} [\frac{2}{As_{Se}}]^{1/2} p_{Zn}^{1/2}$

$$= K_o (\exp \frac{\Delta H_{ZnV} + \Delta H''_F}{2kT})[\frac{2}{As_{Se}}]^{1/2} p_{Zn}^{1/2}$$

Temperature dependence of [e'] at a particular p_{Zn} gave

$\Delta H_{ZnV} + \Delta H''_F = 1.8$ eV. With $\Delta H_{ZnV} = -1$ eV as found earlier,

$\Delta H''_F = 2.8$ eV

This is the enthalpy for the Frenkel disorder process:

$$Zn_{Zn}^x + V_i^x \rightarrow V''_{Zn} + Zn_i^{\bullet\bullet}$$

Should Schottky disorder be dominant, the same value of 2.8 eV would apply to $\Delta H''_S$, the enthalpy of the reaction $O \rightarrow V''_{Zn} + V_{Se}^{\bullet\bullet}$.

A.3 ZnSe:Ga

Investigations on ZnSe + Ga single crystals were carried out because in the literature there is evidence of the observation of p-type conductivity in ZnSe:Ga which is not properly understood.

Attempts to measure high temperature electron concentration in Ga doped ZnSe under Zn pressure were unsuccessful because of bad electrical contacts. Room temperature electron concentrations were measured in samples quenched from high temperature after equilibration at different Zn-pressures. The crystal always showed n-type conductivity. At high Zn pressure electron concentration was found not to vary significantly with Ga content. The electron concentration in ZnSe:100Ga was essentially independent of p_{Zn} at high Zn pressure, but was found to be dependent on the temperature from which the crystals were quenched. More experiments on the ZnSe:Ga system are needed to fully explain the observed behavior.

Attempts to measure high temperature Hall effect under Se vapor were so far unsuccessful because no suitable lead wire was found which can resist chemical attack by Se vapor.

B. An Electron Microscope Investigation of Structural Imperfections in II-VI Compounds (ZnSe and CdTe)

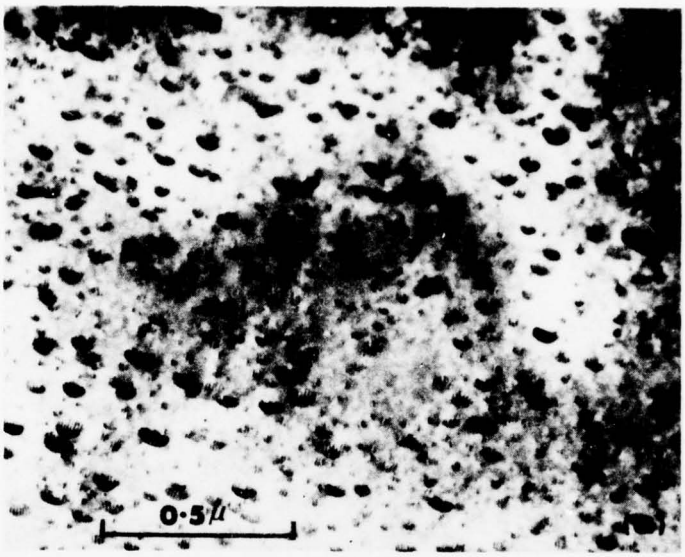
The objective of this research program is to characterize the lattice defects in CdTe and ZnSe by using thin foil transmission electron microscopy and further to examine how the defect structures are influenced by the presence of dopant impurities and by various post-growth annealing treatments. The work in this period was concentrated on the study of ZnSe doped with 100ppm of Ga. The crystals were obtained from Eagle Picher Company and are from the same batch as those used by Professor Kroger and his students in their study of the electrical and optical properties. The crystals were subjected to annealing treatments at 700°C under Zn partial pressures of 10^{-3}, 3×10^{-3}, 10^{-2}, 3×10^{-2} and 1×10^{-1} atmospheres. These heat treatments are identical to those

carried out in the electrical properties studies of the crystal so that a definite correlation between the observed changes in the defect substructure and electrical properties can be attempted.

Thin foils suitable for transmission electron microscopy were prepared from bulk crystals using a chemical jet polishing technique using a solution of 40 parts HCl, 4 parts H_2O_2 and 1 part H_2O by volume. The use of this chemical solution, although produced electron transparent specimens (which under conventional optical examination exhibited high degree of surface finish) when examined in the electron microscope revealed the presence of surface contamination in the form of thin discs or platelets 500 to 1000 Å in diameter. These surface contaminants, in many cases exhibited Moire fringe contrast, a typical example of which is shown in Fig. 1(a). Diffraction patterns obtained from such specimens showed diffused rings resulting from the contaminant in addition to the spot pattern due to ZnSe. Figure 1(b) shows a diffraction pattern obtained from a heavily contaminated region of a thin foil in which a number of rings are clearly visible. An analysis of this ring pattern and moire fringes indicated that the contaminants are probably thin layers rich in zinc. It is believed that such layers could have formed due to the rapid preferential dissolution of Se in the chemical polishing solution.

The extent of such contamination can be minimized by exercising extreme care in washing the samples after chemical polishing (use of warm water seem to help) however total elimination of the contamination was virtually impossible. Short time (2 to 5 minutes) ion beam etching using low energy (1 kV) Ar^+ ions at low beam current may be also used

FIG. 1



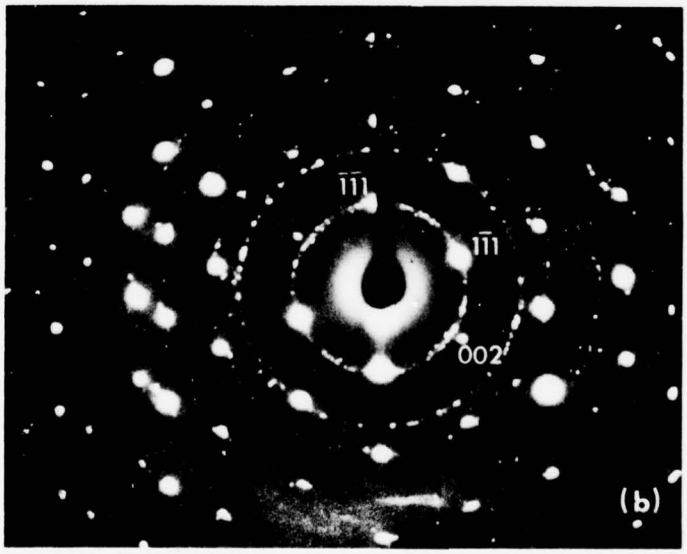


Fig. 1(a) A brightfield micrograph showing surface contaminants on a ZnSe thin foil specimen prepared by using the $HCl-H_2O_2-H_2O$ chemical polishing solution. Note the moire' fringes associated with the surface contaminants.

(b) Selected area electron diffraction from a heavily contaminated specimen showing diffuse rings resulting from the contaminant superimposed on the spot pattern from ZnSe.

to remove the surface contamination after chemical polishing. Use of several other chemical polishing solutions (both acedic and alkaline Eg: A mixture of 0·1BN NaOCl and 0·18N Na_2CO_3 ; 90 gram $K_3Fe(CH)_6$, 1.7 gram KOH in 300 of H_2O ; or 0.4% by volume of Br in methanol) yielded less than satisfactory results.

B.1. Lattice Defects in Ga-doped ZnSe

The microstructure of as-grown ZnSe doped with 100ppm of Ga was virtually free of most lattice defects except for the presence of isolated extrinsic stacking faults. An example is shown in Fig. 2. The average dislocation density in the as-grown crystal was below $10^4/cm^2$. Annealing of the as-grown crystal at 700°C under a Zn partial pressure of 1×10^{-3}atm. showed no substantial changes in the microstructure. A few precipitates were visible in the matrix (see Fig. 3). On increasing the Zn partial pressure to 3×10^{-3}atm., the substructure revealed the presence of a few dislocation loops as can be seen in Fig. 4. These loops, which lie on the {110} planes of ZnSe, showed no fault contrast when imaged under various operating reflection. Using conventional image contrast analysis which is outlined in literature (1) these loops have been identified to be prismatic in nature and of the vacancy type. The formation of an unfaulted prismatic loop on the {110} type of planes in ZnSe requires equal numbers of Zn and Se vacancies. Consequently, the formation of these loops indicate the presence of an excess concentration of both Zn and As vacancies under the conditions of annealing.

700°C annealing under a still higher partial pressure of Zn, viz: $p_{Zn} = 3 \times 10^{-2}$atm., resulted in the formation of a still higher

FIG. 2

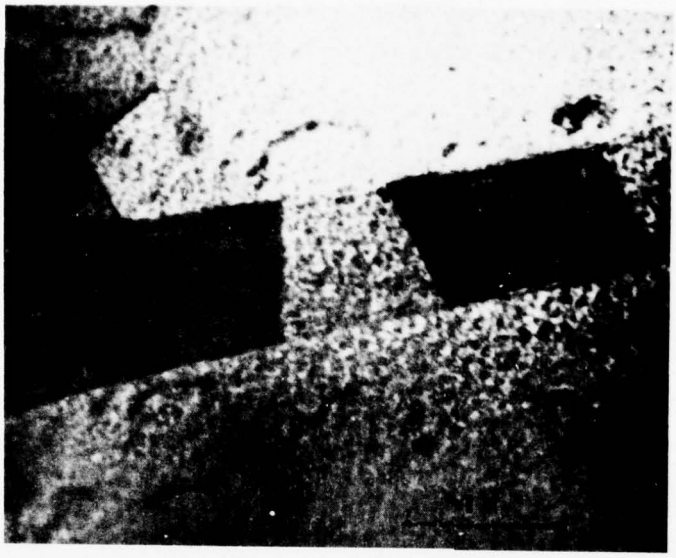


FIG. 3

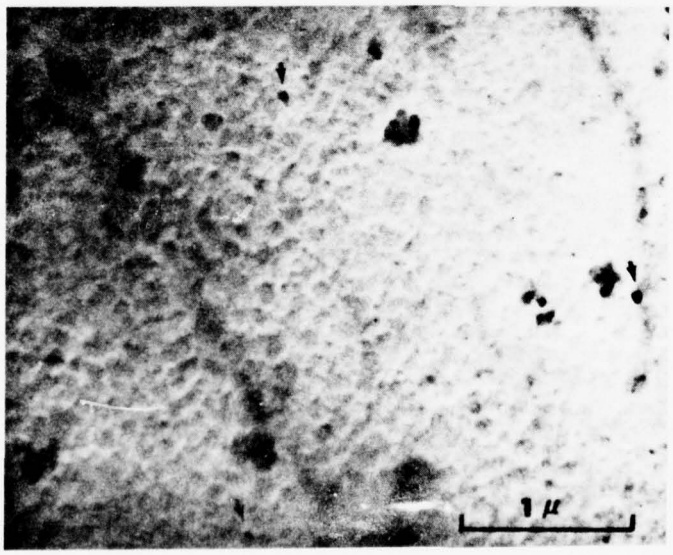


Fig. 2 Brightfield micrograph showing extrinsic stacking fault in the as-grown ZnSe doped with Ga.

Fig. 3 Brightfield micrograph of a Ga-doped ZnSe annealed at 700°C under a Zn-partial pressure of 10^{-3} atoms. Arrows show isolated precipitates.

density of vacancy-type prismatic dislocation loops. A typical example of the resulting substructure is shown in Fig. 5(a). Apart from the circular loops, there appears a number of loops with parallelogram shape. Trace analysis showed that the dislocation segments bounding the parallelogram shaped loops lie along <112> type directions in ZnSe. In addition to the loops which lie on {110} habit planes, there are a number of other loops which lie on {111} planes of ZnSe. As in the case of the samples annealed under $p_{Zn} = 3 \times 10^{-3}$atm., all the loops present in samples annealed under a Zn partial pressure of 3×10^{-2}atm. were also identified to be of the vacancy type. Another feature of the microstructure of these specimens is the presence of helical dislocations. Fig. 5(b) shows the initial stages of the formation of a dislocation helix and Fig. 5(c) shows a helix (marked by the arrow) which has already been formed. The formation of these helices also is an indication of the presence of a concentration of point-defects (possibly vacancies in the present case) in excess of the equilibrium value at this temperature. In addition to the presence of the dislocation loops and helical dislocation in several areas of the speicmens annealed at 700°C under a p_{Zn} of 3×10^{-2}atm. showed dislocation tangles which were associated with an unidentified precipitate. An example of such dislocation tangles is shown in Fig. 5(d). It is believed that dislocations are probably punched out by the precipitate which is harder than the matrix, during cooling from the annealing temperature. On increasing the Zn partial pressure to 0.1atms. there was a drastic reduction in the density of the prismatic loops. However, the unidentified precipitates and the dislocation tangles associated with them were still present in the

FIG. 4

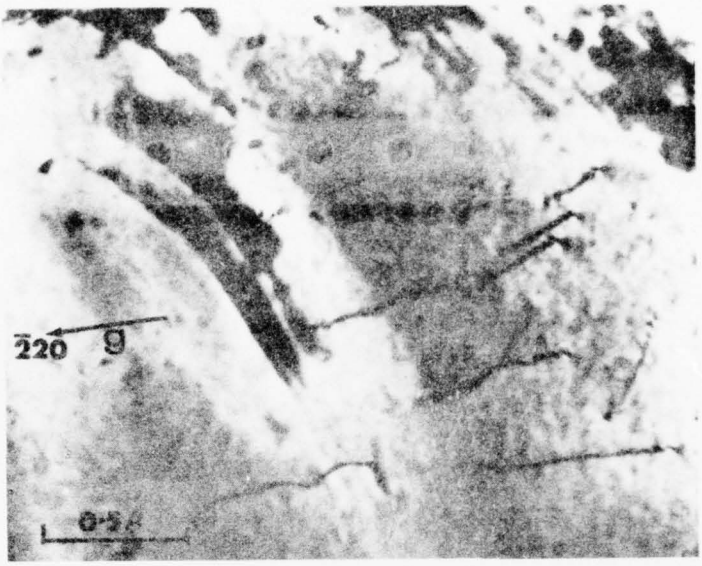
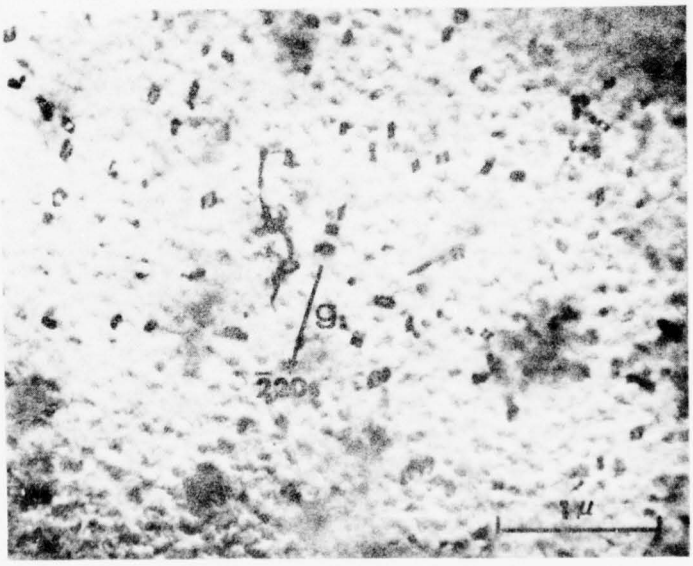


FIG. 5

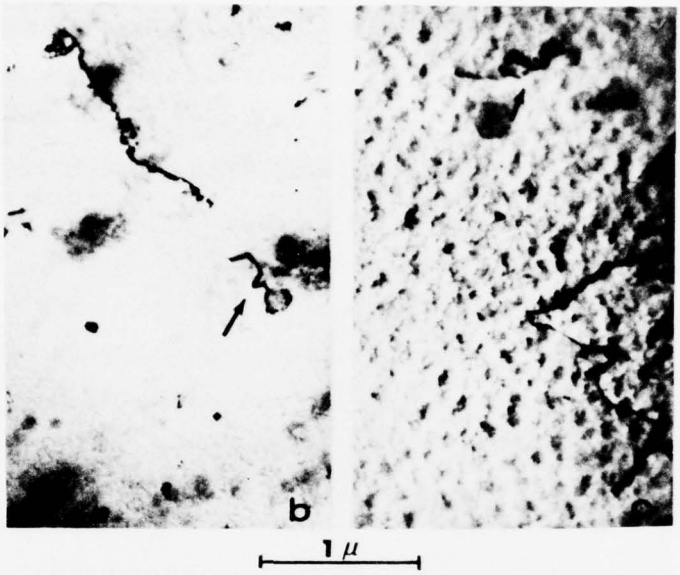


a

Fig. 4 Brightfield micrograph showing the presence of prismatic dislocation loops in a Ga-doped ZnSe sample annealed at 700°C under a Zn-partial pressure of $3x10^{-3}$ atms.

Fig. 5(a) Brightfield micrograph showing the distribution of vacancy type prismatic loops in Ga-doped ZnSe following a 700°C anneal under a Zn partial pressure of $3x10^{-2}$ atms.

FIG. 5



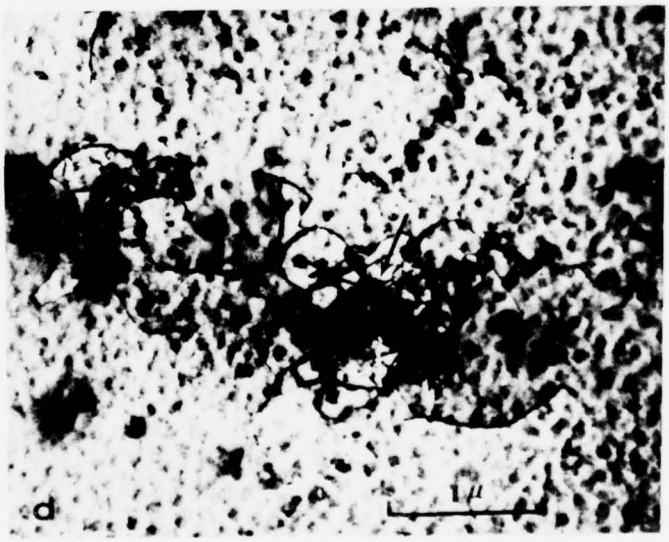


Fig. 5(b) Brightfield micrograph showing the initial stages of formation of a dislocation helix (arrow) in the same sample as that in Fig. 5(a).

(c) Brightfield micrograph showing a fully transformed helix in the same sample as above.

(d) Brightfield micrograph showing dislocation tangles associated with unidentified precipitates (arrow) in the sample annealed at 700°C under a $P_{Zn} = 3 \times 10^{-2}$ atms.

microstructure, as can be seen in Fig. 6.

The annealing induced changes in the substructure of Ga-doped ZnSe, reported above are currently being analyzed in the light of the defect model developed by Professor Kroger and his students based on their electrical properties measurements on this system. The formation of the dislocation loops occurs in the same Zn partial pressure range at which the change in electron concentration with p_{Zn} shows a discontinuity [2]. Such a discontinuity seems to indicate the occurrence of some carrier compensation mechanism that may be linked to the formation of prismatic dislocation loops. It is interesting to note that formation of vacancy type prismatic loops during annealing has been observed previously in donor-doped GaAs, with accompanied decreases in free carrier concentration [3,4].

C. Absorption Studies of CdTe and ZnSe

During the past year our efforts to investigate impurity and defect-related absorption in CdTe and ZnSe have continued. The work has been concentrated on three main problems. The first was completion of the vibrational mode absorption of P (phosphorus) in CdTe, second was the extension of the CdTe:P study to the P-doped ternary materials $Zn_xCd_{1-x}Te$ and $Mg_xCd_{1-x}Te$ and third was the completion of our study of absorption by free electrons in Al-doped ZnSe.

The CdTe:P work was largely reported in the 1975 annual report and will be published in the Journal of Applied Physics. The major findings of this study were: 1) there are two P defect centers, one P_{Te} or P_i center having T_d symmetry and the other a P-complex with axial symmetry; 2) the P_{Te} or P_i is a shallow acceptor, while the P-complex appears to be a neutral center; 3) the shallow acceptors P_{Te} or P_i are present in unassociated form and native donors, such as Cd interstitials, account for the observed self-compensation.

The second and third studies referred to above have also been completed, submitted and accepted for publication in the Journal of Applied Physics. Since there is relatively little detail on these studies in previous reports we present the results in the two papers which are included as Appendices A and B.

FIG 6

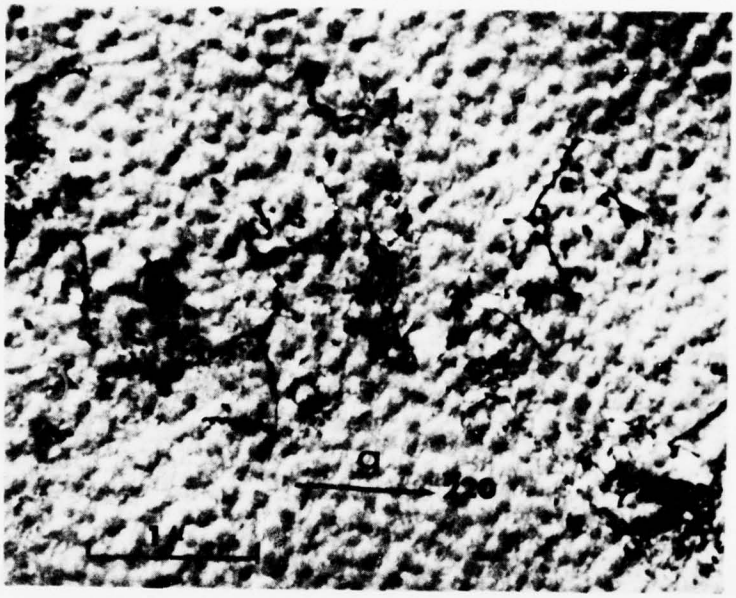


Fig. 6 Brightfield dislocation showing the presence of precipitates and decorated dislocations (arrow) in a Ga-doped ZnSe annealed at 700°C under a Zn-partial pressure of 0.1 atm.

III. PULSED LASER INDUCED DAMAGE

(M. Bass, K. M. Leung, C. C. Tang)

A. Re-examination of Laser Induced Breakdown in the Alkali Halides at 10.6 μm

1. Introduction

The laser induced bulk damage thresholds of IR materials have been shown to depend upon the manner in which the samples are irradiated [5]. In reference [5], it is reported that sites in a sample which have been pretreated by low laser intensities will have higher damage thresholds than unconditioned sites. Other investigators [6] have also observed this effect. Since the damage thresholds of alkali halides have been used to identify avalanche breakdown as the intrinsic damage mechanism [7], the results of references [5] and [6] indicate the need for remeasuring the damage properties of these materials. This requires re-examining the procedure of irradiation used by various researchers in measuring breakdown thresholds. In this section, we discuss the variations in damage thresholds between different samples of the same material. We present data which show that the dependence of the damage threshold on the method of irradiation is related to the presence of defects and inclusions in the medium. To determine the exact role of defects in laser induced breakdown of materials, a study was also made of 1) the relationship between the damage threshold and the size of the irradiated focal volume, and 2) the damage thresholds of recent conventional and RAP grown samples as compared to previous samples of the same materials.

2. Experimental

The experimental set up used has been described in detail earlier [8]. High speed photon drag detectors were used for comparing the incident laser pulse waveform with that transmitted through the sample. The occurrence of damage was visually determined during the experiment by the occurrence of a spark or by the appearance of residual damage

following irradiation. An optical microscope was used later to examine the morphology of each irradiated site. Physical damage was accompanied by an attenuation of the transmitted pulse. The damage threshold was defined as the incident flux at which 50% of the irradiated sites damaged and its value was determined from the average of the results for 10 sites.

The important parameters of the TEA CO_2 laser system are summarized in Table I. The laser was operated in the fundamental TEM_{00} transverse mode in order to provide a well characterized beam spatial profile. This was focused into the bulk of the samples with lenses resulting in focal spot diameters of 59 μm or 89 μm. In our experiments, the diameter is defined as the diameter at which the intensity falls to $1/e^2$ of its peak value. Consistent with the notation used in the literature, this definition corresponds to the diameter at which the electric field falls into 1/e of its peak value. Since damage only occurs in the first half of the gain-switched CO_2 laser pulse as evidenced by observation of the transmitted waveform [8], the long tail of the pulse, containing 50% of the total energy, does not contribute to the breakdown mechanism of the

Table I. Summary of Experimental Parameters

Laser	CO_2 TEA
Wavelength	10.6 μm
Waveform	92 nsec gain switched pulse with self mode locked spikes $\lesssim$2.5 nsec duration and 8 nsec interpulse spacing
Transverse mode	TEM_{00}
Attenuation	ZnSe beam splitter and two Brewster angle stacked plate polarizers
Focusing lens	Ge, 2.54 cm and 3.8 cm focal lengths, abberation free
Focal spot diameter	59 μm and 89 μm at $1/e^2$ in intensity
Detection system	Photon drag detectors and Tektronix 7844 oscilloscope. Risetime = 2.5 nsec.

material. The average energy flux $\tilde{\mathcal{E}}$ (J/cm^2) is given by

$$\tilde{\mathcal{E}} = \frac{\frac{1}{2}\mathcal{E}}{\pi w_0^2}$$

where $\mathcal{E}$ is the total energy contained in the entire pulse. The average power density P(W/cm^2) and the peak on-axis power density P_0(W/cm^2) are then related by

$$P_0 = 2P = 2\ \tilde{\mathcal{E}}/\tau$$

where τ is the full width at half maximum of the gain-switched part of the TEA laser pulse.

3. Comparison of N on 1 and 1 on 1 Damage Thresholds

An N on 1 measurement of the laser damage threshold has been defined as one in which a site is initially irradiated at a low intensity and the flux is increased by a small amount (5% in these experiments) on successive pulses until damage occurs [5]. This was the procedure used by Allen et al. [6] in reporting damage thresholds for RAP grown alkali halides. A more conventional threshold measurement is obtained in a 1 on 1 experiment where each site is irradiated only once and the intensity which produces damage 50% of the time is sought [5, 7, 8].

Our data for the N on 1 and 1 on 1 thresholds of several materials is summarized in Table II. We note that the differences are not due to the difference in the definitions of the N on 1 and 1 on 1 thresholds because by increasing the incident flux by only 10% in a 1 on 1 experiment, we could produce damage on all sites. Thus, a difference greater than 10% is indicative of a conditioning effect due to the low intensity pulses in an N on 1 test.

Table II shows that the N on 1 experiment gives noticeably greater thresholds in the RAP processed KBr and the conventionally grown KI. The difference is less in KCl and in NaCl and NaF the two thresholds are the same. A few of the samples had very low thresholds due to high

Table II. Comparison of N on 1 and 1 on 1 Laser Damage Thresholds

Material	10.6 μm Damage Threshold in GW/cm^2		Spot Size $2w_0$ = 89 μm
	1 on 1	N on 1	$R = \frac{I_{Threshold}\ (N\ on\ 1)}{I_{Threshold}\ (1\ on\ 1)}$
NaCl (conventional)	9.83	9.89	1.00
NaCl (RAP)	<.38	<.38	- -
KCl (conventional)	.87	1.13	1.3
KCl (RAP)	<.38	<.38	- -
KBr (conventional)	<.38	<.38	- -
KBr (RAP)	7.23	15.35	2.12
NaF (conventional)	16.49	17.07	1.04
KI (conventional)	1.07	1.97	1.84

concentrations of inclusions and so in Table II their damage fluxes are given as upper bounds. The presence of inclusions or defects in certain samples was detected by the observation that the positions of the damage sites varied randomly along the incident beam direction. In particular, this was seen in the RAP processed NaCl and KCl samples used in the present study. We note that as a result these samples had lower damage thresholds than conventionally prepared samples of NaCl and KCl. The reverse is true for the samples of KBr studied in this work.

4. Comparison of Materials

Upon comparing the thresholds of these materials with other samples investigated by Bass and Leung [5], a marked increase in damage

thresholds for the conventionally grown NaCl and KCl samples was noted. The thresholds which they obtained for conventional NaCl and KCl were 6.10 GW/cm^2 and .65 GW/cm^2 respectively as compared to 9.83 GW/cm^2 and 0.87 GW/cm^2 obtained herein. The previous RAP grown KCl had a threshold of 4.60 GW/cm^2 which is significantly higher than that of the sample studied in this work. This indicates that RAP grown materials are not necessarily always better than conventional materials. Clearly, they could be more damage resistant than conventional materials if they are inclusion and defect free.

A comparison of the breakdown electric fields of the recent samples with those obtained by Yablonovitch [7] at 10.6 μm is shown in Table III. The electric fields are normalized to that of NaCl. In the

Table III. Relative Breakdown Fields at 10.6 μm - Normalized to E_{NaCl}

Material	Current Results	Previously Published Results
NaCl	1	1
KCl	.573	.713
KBr	.309	.482
NaF	1.33	1.64 (@1.06 μm) [9]
KI	.440	.27

present work and for our particular sample of NaCl, the breakdown electric field was found to be (1.8 ± 0.18)MW/cm. Our experimental conditions were nearly identical to those of Yablonovitch who obtained (1.95 ± .2) MV/cm for the breakdown field of NaCl at 10.6 μm [7]. We can see that the two results agree within the experimental of the measurements. Table III shows that there is general agreement in the breakdown field ratios for KCl and NaF. For the other samples, however, the ratios differ widely. Since the agreement of the results for NaCl indicates adequate experimental accuracy, we conclude that the discrepancies in the electric field ratios for the same materials are due to sample variations. This suggests that the damage threshold for any material should be obtained from the average of the value

obtained for several samples

5. Dependence of Damage Thresholds on Spot Size

DeShazer, Newnam and Leung [10] have previously reported that the damage thresholds of thin optical coatings correlate strongly with the size and distribution of defects. Since the probability of hitting a randomly distributed defect is greater when a large cross-sectional area is irradiated than when a smaller area is irradiated, and since materials containing defects damage more easily than defect free materials, it is to be expected that large diameter beams, on the average, damage materials more easily than small diameter beams. The present work extends the results of [10] to bulk damage in transparent materials.

In order to investigate the role of defects in solids, the power density thresholds for damage to the materials shown in Table IV were determined using two lenses (their focal lengths were 25 and 38.0 mm) yielding focal spot diameters of 59 μm and 89 μm. The thresholds for NaCl, NaF and RAP KBr did not depend noticeably on the focal spot

Table IV. Comparison of Damage Thresholds for Different Spot Sizes

Material	10.6 μm Damage Threshold in GW/cm^2	
	$2w_0$ = 59 μm	$2w_0$ = 89 μm
NaCl	13.21	9.83
NaCl - RAP	3.30	<.38
KCl	2.92	0.87
KCl - RAP	3.21	<.38
KBr	0.88	<.38
KBr - RAP	7.83*	7.23
NaF	19.02	16.50
KI	1.91	1.07

*preliminary data

diameter. For other samples, such as RAP NaCl and RAP KCl, the damage thresholds using the different lenses differed by an order of magnitude. Due to the smallness of the RAP KBr sample, only preliminary data consisting of a single site could be obtained using a 59 μm spot size.

The presence of defects in RAP KCl and NaCl was verified by morphological studies. The samples showing no dependence on focal spot diameter were either densely filled with small inclusions or relatively inclusion free and damaging due to an intrinsic process.

B. Pulse Laser Damage in Three Layer 10.6 μm AR Coatings on KCl

1. Introduction

One goal of the IR Window Program is to develop 10.6 μm antireflection (AR) coatings for KCl window materials such that the absorption, reflectance and scattering losses are each less than 0.1% per surface. It is also necessary for the coatings to have good environmental stability and a high laser damage threshold.

Previous studies [11] had shown that these goals could not be achieved using two layer designs. Thus, several three layer designs were generated at Hughes Research Laboratory (HRL). Preliminary studies indicated that these AR coatings could meet the program goals for absorption and reflection losses. The experimental studies have been extended to other designs and these AR coatings have been subjected to pulsed laser damage measurements in this work.

2. Experimental

The experimental procedure used in the damage measurements was described in detail in references [8] and [12] and in the preceding section. The following derivation of the expressions for peak on-axis intensity, energy density and etc. is included here for completeness. The relationships between the desired quantities and the measured total energy, pulse duration and focal spot radius can be derived in the following manner:

A laser pulse which has Gaussian spatial and temporal profiles will have an instantaneous power density of the form

$$P(r,t) = P_o \exp\left((-4\ln 2)t^2/\tau^2\right) \exp(-2r^2/w_o^2)$$

where r and t are the radial and time coordinates. The symbols are defined in the list of symbols in Table V. The total energy contained in the pulse is

$$E_{total} = \int_{-\infty}^{\infty} \int_{-\infty}^{\infty} \int_{-\infty}^{\infty} P(r,t)\,dt\,dx\,dy$$

where $r^2 = (x^2 + y^2)$. Carrying out the integration over t gives

$$E_{total} = \int_{-\infty}^{\infty} \int_{-\infty}^{\infty} \left[\frac{P_o \tau}{2}\sqrt{\frac{\pi}{\ln 2}}\right] e^{-2r^2/w_o^2}\,dx\,dy.$$

The term in brackets is just the peak on-axis energy density and so

$$\mathcal{E}_o = \left[\frac{P_o \tau}{2}\sqrt{\frac{\pi}{\ln 2}}\right] = \frac{P_o \tau}{0.94} \,. \tag{1}$$

The total energy is then

$$E_{total} = \int_{-\infty}^{\infty} \int_{-\infty}^{\infty} \mathcal{E}_o\, e^{-2r^2/w_o^2}\,dx\,dy$$

$$= \mathcal{E}_o \frac{\pi w_o^2}{2} \,. \tag{2}$$

Using Eqs. (1) and (2), we obtain the following relation between the desired and the measured quantities:

$$\mathcal{E}_o = \frac{2E_{total}}{\pi w_o^2} \tag{3}$$

$$\bar{\mathcal{E}} = \mathcal{E}_o/2 \tag{4}$$

$$P_o = \frac{0.94}{\tau} \quad \mathcal{E}_o = \frac{0.94}{\tau} \quad \frac{2\,E_{total}}{\pi\, w_o^2} \tag{5}$$

$$\overline{P} = P_o/2 \tag{6}$$

Table V.

P_o	≡	Peak on-axis power density (W/cm^2)
$\overline{P}$	≡	Average power density (W/cm^2)
$P(r,t)$	≡	Instantaneous power density (W/cm^2)
$\mathcal{E}_o$	≡	Peak on-axis energy density (J/cm^2)
$\overline{\mathcal{E}}$	≡	Average energy density (J/cm^2)
E_{total}	≡	Total energy (J)
τ	≡	Pulsewidth (FWHM) of gain-switched pulse)
w_o	≡	Radius of beam at $1/e^2$ point in intensity

3. Results

The coatings tested in this study are described in reference [11] and were deposited on KCl substrates. The ZnSe/ThF_4/ZnSe design was developed first. Of 19 samples, six had an absorption loss of 0.05 to 0.06% per surface, six had losses of 0.07 to 0.085% and three were in the range of 0.09 to 0.10%. Of the same group, eight had reflectance losses of less than 0.06% and three had losses in the range of 0.07 to 0.10% per surface.

The ZnSe/KCl/ZnSe design was tested next. The films had a higher absorption than predicted. They exhibited an opalescent appearance which may be due to crystallite formation of the KCl layer. A number of runs were made to determine if modification of the substrate deposition temperature or the deposition rate would eliminate this feature. No significant differences were observed for substrate temperatures of

25 to 110°C and a three fold variation in the deposition rate. A total of 16 samples were prepared. These had an average reflectance loss of 0.06% (the range was 0.04 to 0.10%), and an average absorption loss of 0.24% (the range being 0.18 to 0.34%).

The coatings that were to be tested were picked up at HRL at 11:00 A.M. on a day in June when the outside temperature was ~90°F. They were packed in sealed boxes with desicant present and at the indoor temperature of ~72°F. It took ~1 hour to transport the samples from HRL to USC where, in the ~72°F temperature of the laboratory the samples were allowed to equilibrate overnight. When they were opened for inspection the next day, all showed signs of crazing. An example of this is shown in Fig. 7 for a ZnSe/ThF/ZnSe sample (HRL #B109 RF3). The dark spot in the center of the micrograph is a laser damage site and was not the cause of the crazing. At this time we attribute such crazing to the thermal cycling which occurred when the samples were brought to USC. The HRL group is working on this problem.

The results of the laser damage threshold tests are presented in Table VI. In the N on 1 test, the laser power was increased in approximately 5% increments at a fixed place until damage was seen to occur. The 1 on 1 test was conducted by exposing the coating to a single laser shot to determine the level at which 50% of the shots result in damage. The differences in the two results are within the range of values and are not considered to be significant.

The damage sites were examined after irradiation with a light microscope to check on the role of defects in the damage process. Figure 8 shows the morphology of a damage site on a ZnSe/KCl/ZnSe coating on KCl. Within the spot corresponding to the irradiated area, the irregularly placed, localized damage sites are considered to be clear evidence of defect induced damage. Notice that in the region near the defect site the coating has been completely removed and the substrate is exposed.

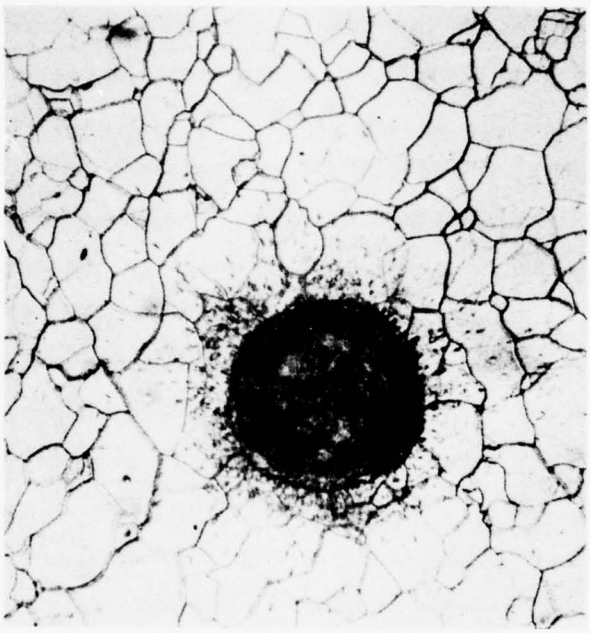
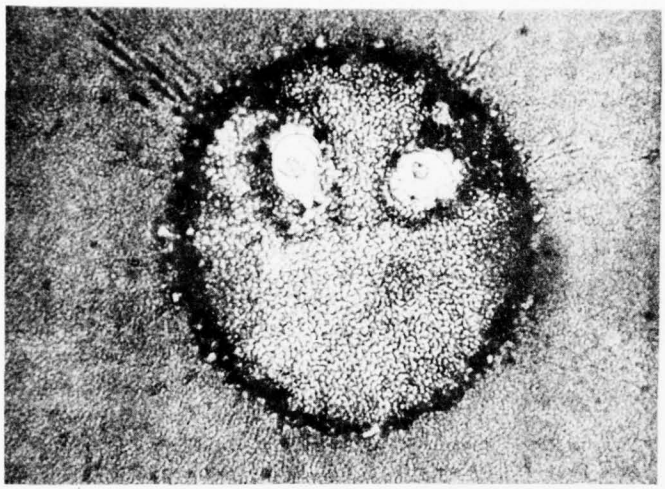


Figure 7. Micrograph of ZnSe/ThF_4/ ZnSe coating on KCl showing crazing caused by thermal cycling. The spot in the photo is a pulsed laser induced damage site produced on the coating after the crazing occurred.

Table VI. Results of Laser Damage Tests

Sample No.	Coating	Reflectance Percent Per Surface	Absorption Percent Per Surface	Type of Test	Average Energy Density, J/cm^2	Peak On Axis Power Density MW/cm^2	Number of Test Sites	Range, MW/cm^2
B109RF2	$ZnSe/ThF_4/ZnSe$	0.06	0.043	N on 1	25.4	520	12	419 to 717
				1 on 1	22.6	463	5	437 to 468
B142B2	ZnSe/KCl/ZnSe	0.03	0.26	N on 1	26.8	549	7	468 to 812
				1 on 1	24.4	500	4	468 to 512
B45-BF1	ZnSe/KCl/ZnSe	0.06	0.22	N on 1	24.0	491	6	437 to 636
				1 on 1	21.1	431	21	413 to 512



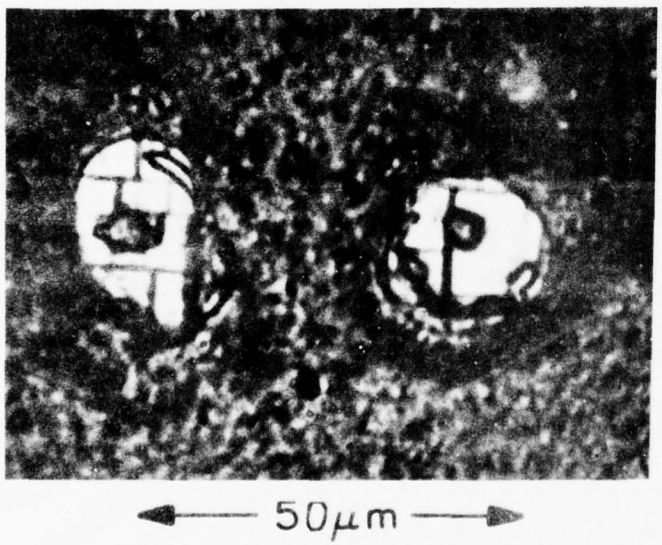


Figure 8. Laser damage to a ZnSe/KCl/ZnSe on KCl A-R coating showing the role of defect (probably absorbing inclusions) in the damage process.

The damage test results reported here, obtained at the Center for Laser Studies, were corroborated by damage measurements taken at Hughes Research Laboratories by V. Wang using a well characterized 10.6 μm pulsed CO_2 laser [13].

C. Pulsed Laser Induced Damage at the DF Laser Wavelength*

1. Introduction

Alkaline-earth fluorides have been studied for use in optical components in laser systems operating in the spectral range from 2-5 μm. The damage resistance of optical materials suitable for use in the 2-5 μm region has not yet been systematically evaluated. In this section we present preliminary measurements of the damage resistance of the best obtainable samples of certain alkali-earth fluorides, alkali-halides and sapphire. We also discuss the properties of these materials as they relate to high power 2-5 μm laser systems.

2. Experimental

The experimental set up and procedures are similar to those described in reference [8]. The basic apparatus consists of a pulsed TE DF laser, a beam attenuator, a test chamber, and an energy/waveform monitoring system. The experimental parameters are summarized in Table VII. The pulsed DF laser used in this work has an unstable resonator cavity and a multiline output of ~400 mJ.

Due to multiline operation, we observed the two peaked waveform from the DF laser shown in Fig. 9. If the laser was operated in a single-line, then a single peak waveform was obtained. However, the energy output of this single-line laser was too weak for our purposes.

In order to define the damage flux of the laser pulse we constructed an equivalent pulse having a single-peak waveform with its maximum equal to that of the second peak and with leading and trailing edges drawn

---

* This part of our research was conducted jointly with M. J. Soileau at Naval Weapons Center, China Lake, California.

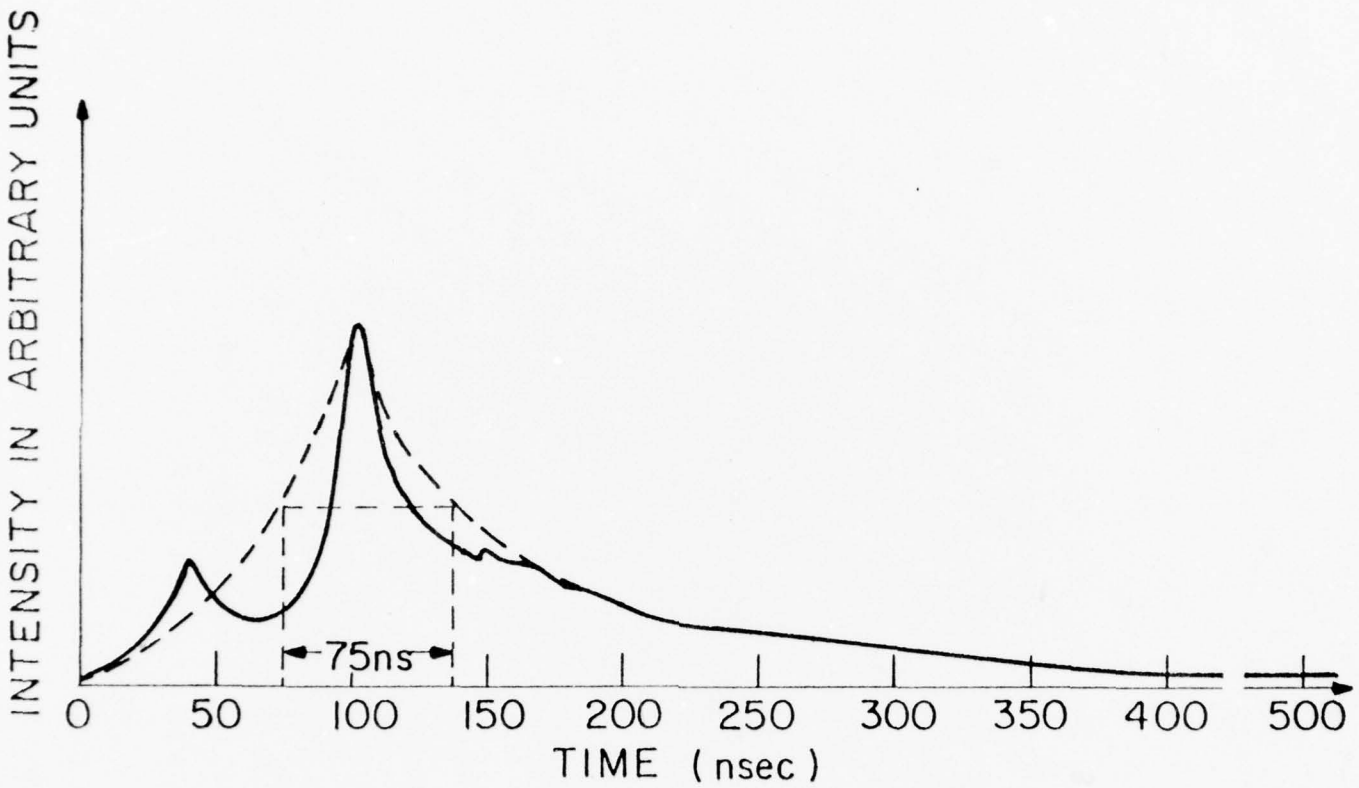


Figure 9. Temporal profile of a multi-line DF laser pulse. The dashed curve represents the equivalent pulse constructed in order to deduce a damage threshold intensity.

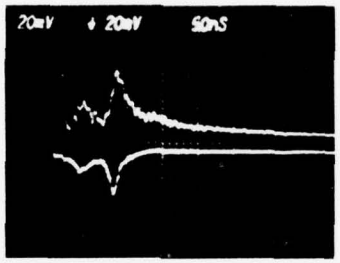
Table VII. Summary of Experimental Parameters

Laser	TE - DF
Wavelength	30 lines (3.5-4.1 μm); 3 dominant lines @3.8 μm each separated by ~0.038 μm
Waveform	2 leading sharp peaks followed by a long low tail, equivalent pulsewidth is 75 nsec
Transverse mode	Lowest order unstable resonator mode
Attenuation	NaCl beam splitter and two ZnSe Brewster angle stacked plate polarizers
Focusing lens	ZnSe, 3.58 cm focal length, AR coated @3.8 μm
Focal spot diameter	120 μm at $1/e^2$ in intensity
Detection system	Photon drag detectors and Tektronix 7844 oscilloscope; risetime = 2.5 nsec

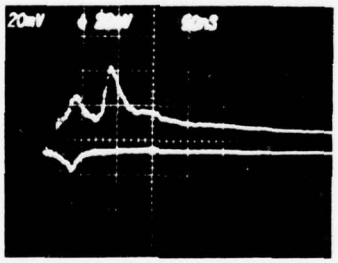
to average out this enclosed area under the original waveform. This equivalent waveform is indicated by the dashed curve in Fig. 9. It contains 50% of the energy that was in the pulse and has a full width of the half maximum of 75 nsec.

We monitored the waveforms of both the incident and transmitted pulses in the manner described in reference [8]. The transmitted pulse was attenuated when damage occurred as shown in Fig. 10. Near threshold, the attenuation occurs at the peak of the second pulse while above threshold it occurs at the peak of the first pulse. This is evidence for the importance of the peak intensity in the damage process. It is also one rationale for constructing the equivalent pulse as described above in order to define the damage flux.

Another problem encountered in our experiment was that due to the unstable resonator cavity configuration, the transverse mode output of the DF laser was an annular ring in the near field [14]. Only in the far field, about 10 meters away from the DF laser, would the mode consist of a near-diffraction limited central spot plus a series of weak secondary annular rings. The experiment in this work was located in



NEAR
THRESHOLD



ABOVE
THRESHOLD

Figure 10. Typical oscilloscope traces for bulk damage in SrF_2 due to DF laser light. The upper trace is the incident pulse waveform and the lower trace is the transmitted pulse waveform. When damage occurs the transmitted pulse waveform is attenuated.

the near field of the DF laser output because of limited laboratory space. As a result of placing a focusing lens in the near field, the determination of the focal spot diameter was more nontrivial than in other circumatances.

Three different approaches were used to estimate the focal spot diameter of the DF laser beam when focused by a 3.58 cm focal length lens. The results of these three approaches which agree very well with each other are summarized in Table VIII. In the first approach, the burn patterns produced by the focused DF laser beam on an anodized aluminum

Table VIII. Determination of Focal Spot Diameter for DF Laser and 3.58 cm Focal Length Lens

1.	By burn on anodized aluminum	130 μm
2.	By scanning 23 cm focal length lens focal spot and scaling according to the ratio of focal lengths	118
3.	By diameter of region of surface damage showing interference "ripples"	< 150

block were measured. The laser energy was varied until the size of the burn pattern became constant but before massive disruption occurred. Using this definition of the measured focal spot diameter we obtained a value of 130 μm. In the second approach, a small pin-hole of 35 μm in diameter was used to scan the focus of a long focal-length lens. The focus of the 3.8 cm focal length lens was not scanned because the focused laser beam readily damaged the pin hole. Instead, we scanned the focus of a long focal-length lens (f = 23 cm) and scaled the result to the short lens according to its focal length. The expected Gaussian spatial profile of the focused beam was observed at the focus of the long focal-length lens. The result of scaling to the short focal-length lens gave 118 μm for the diameter at the $1/e^2$ points of intensity. In the third approach, we measured the diameter of a surface damage site showing interference ripples [15]. These ripples are produced when dust particles, defects or inclusions, at or near the surface scatter light which then interferes

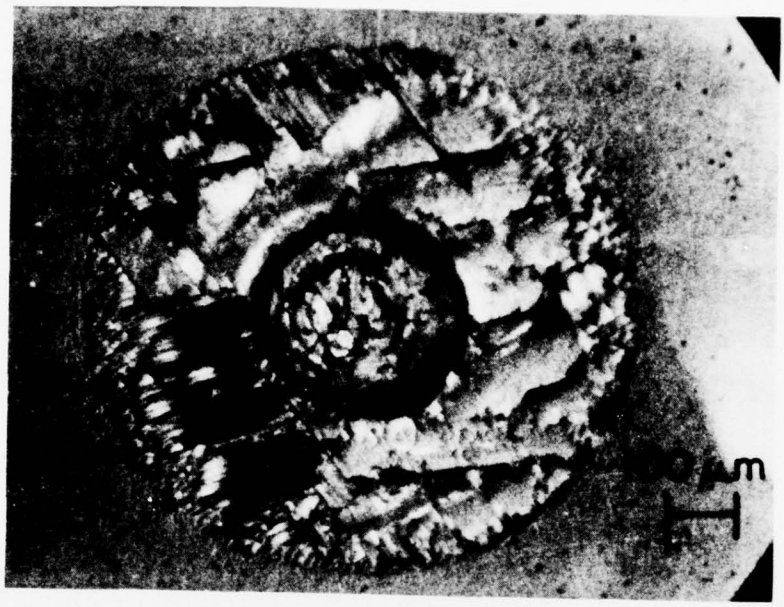
with the incident light. The resulting interference pattern is seen in the damaged material only in the region directly exposed to the incident beam. The parts of the damage sites showing interference ripples were found to be less than 150 μm in diameter. This observation is illustrated in the micrographs shown in Fig. 11.

3. Damage in the 2-5 μm Optical Materials

Several types of damage morphology were observed on both the entrance and exit surfaces of the tested samples. Figure 11 is a micrograph of a damage site located at the exit surface of a SrF_2 crystal. (Nomarski illumination was used to obtain the micrographs presented in this section.) The central region in Fig. 11 contains interference ripples and is the area directly irradiated by the DF laser pulse. The diameter of this region in which the damaging interaction took place is ≈150 μm. The extended area showing massive disruption results from the response of the medium to the violent interaction that took place in the irradiated area.

Almost all damage sites on the surfaces of the alkaline-earth fluorides show aligned cracks corresponding to the cleavage planes of the crystals. Figure 12 shows a damage site at the entrance surface of a CaF_2 crystal. A distinctive family of aligned cracks can be seen oriented in a preferred direction within the site. However, on the same crystal, another damage site shows two sets of cracks having two different orientations as seen in Fig. 13. The dividing line which we thought was a polishing scratch is actually the edge of a twin plane. On one side of the edge, the cracks are oriented with respect to the cleavage plane of one twin and on the other side, they are oriented according to the cleavage plane of the other twin. For a MgF_2 crystal, which has no well defined cleavage plane, no oriented cracks were observed as shown in Fig. 14.

Although no pictures are available to show the bulk damage morphology, we observed that for most of the fluoride materials, the damage



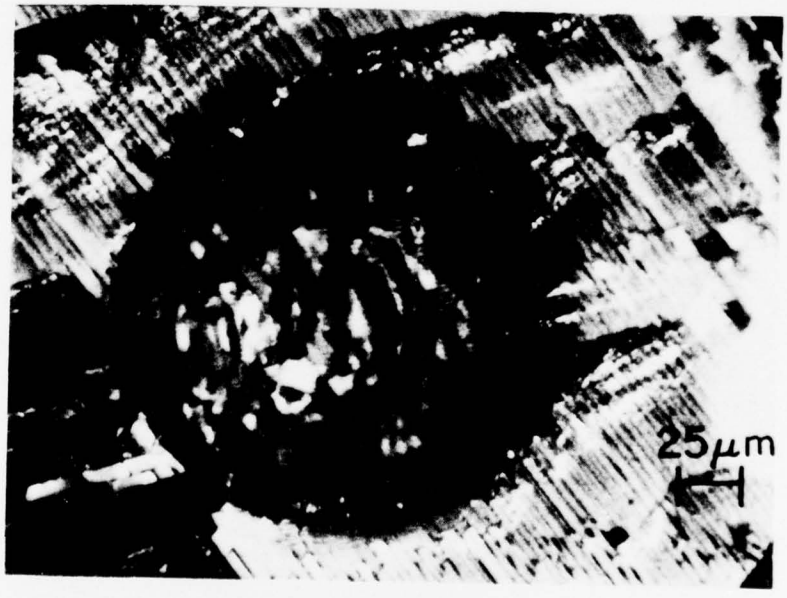


Figure 11. Nomarski micrographs of exit surface damage to SrF_2. The lower photograph is an enlargement of the central region of the irradiated site showing interference ripples.

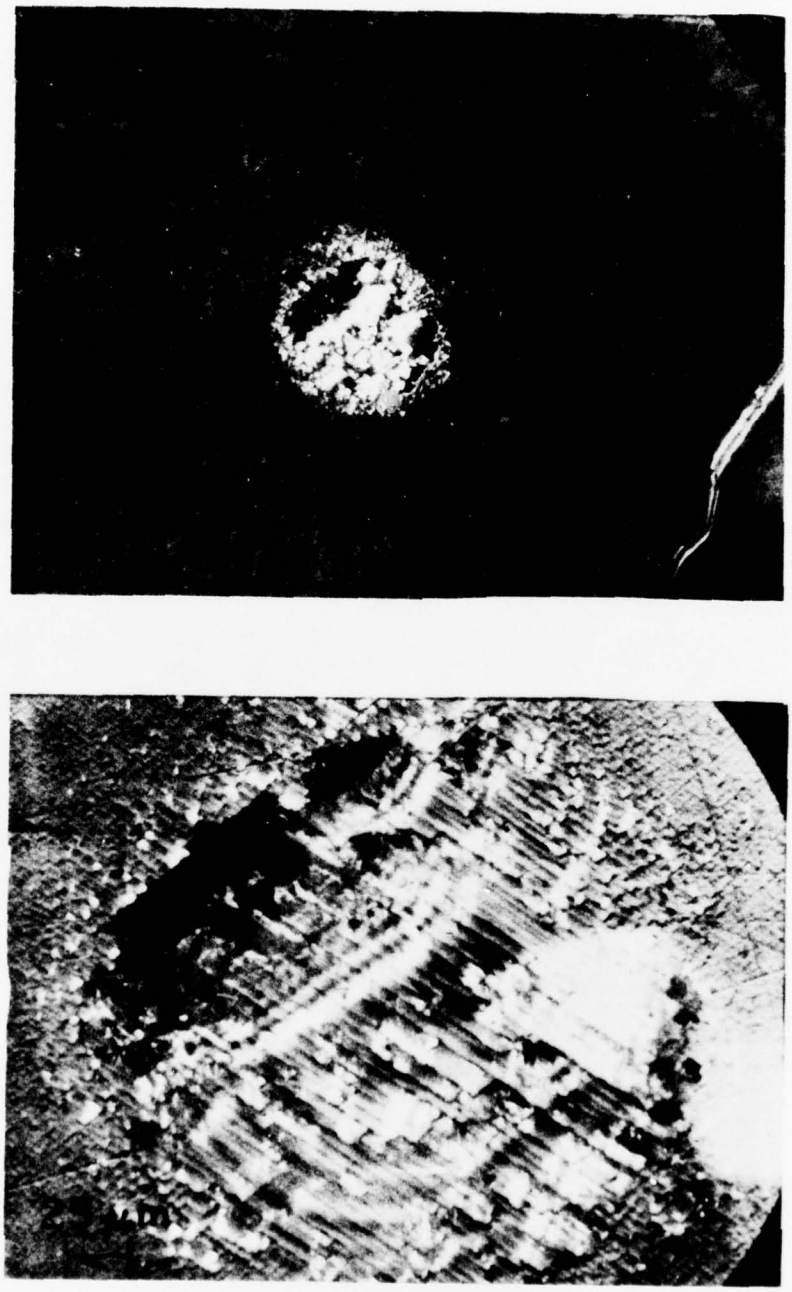


Figure 12. Nomarski micrographs of entrance surface damage to CaF_2. The lower photograph is an enlargement of the damage site showing the aligned cracks.

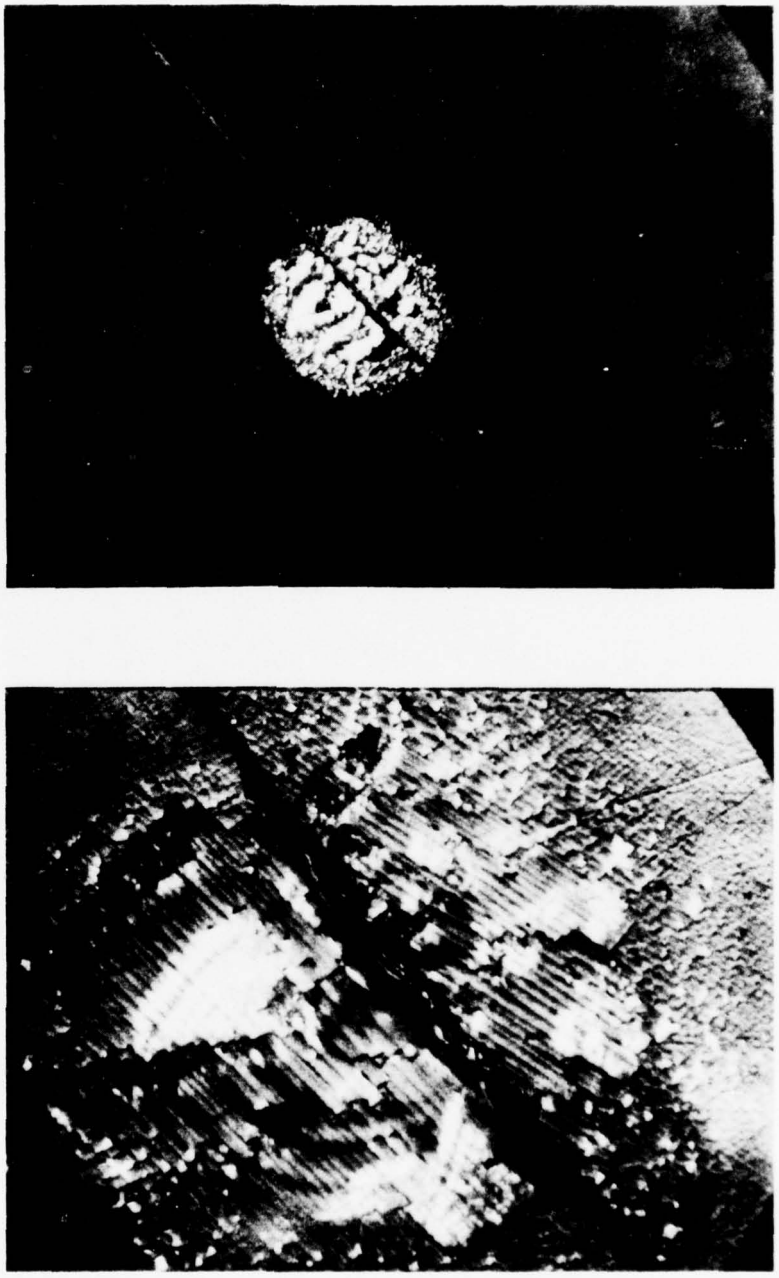


Figure 13. Nomarski micrographs of entrance surface damage to the same CaF_2 crystal as in figure 12. The enlarged picture shows clearly the edge of a twin plane which divides two sets of aligned cracks.



Figure 14. Nomarski micrographs of entrance surface damage to a MgG_2 single crystal. No aligned cracks are observed in this case since MgF_2 has no well defined cleavage planes.

site locations varied along the axis of the incident laser beam. This suggests that the damage mechanism in the samples that we have studied is determined by the presence of defects or inclusions.

Several important physical properties of the 2-5 μm materials which we studied are listed in Table IX. In general, the alkaline-earth

Table IX. Some Properties of Potentially Useful 2-5 μm Materials

	Index of Refraction n	Average Sample's Absorptivity[a] $\beta(cm^{-1})$	Knoop Hardness	Melting Point °C
Alkaline-Earth Fluorides				
MgF_2	1.355	4.8×10^{-4}	415	1255
CaF_2	1.41	$\sim 3.5 \times 10^{-4}$	120	1395
SrF_2	1.41	$\sim 6 \times 10^{-4}$	130	1450
BaF_2	1.457	$\sim 18.5 \times 10^{-4}$	65	1355
Alkali-Halides				
LiF	1.353	25.5×10^{-4}	102	844
NaF	1.31	5.2×10^{-4}	60	1012
NaCl	1.52	4.2×10^{-4}	18	801
Al_2O_3	1.68	4×10^{-2}	~1700	2040

[a] These values are taken from references [16] and [17].

fluorides have absorption coefficients of $\sim 10^{-4} cm^{-1}$. On the other hand the absorption of sapphire is two orders of magnitude higher than that of the alkaline-earth fluorides.

If damage in these samples is determined by the presence of defects or inclusions, one might expect low damage threshold to correlate with high scattering at the laser wavelength. Therefore, we measured the total scattering for these samples at four different

wavelengths including 3.39 μm which is sufficiently close to the DF laser wavelength (~3.8 μm) to permit a comparison of scattering and damage. The results of our scattering measurements are given in Table X.

4. Results of Damage Threshold Measurements

The bulk damage thresholds for the materials we studied are listed in Table XI. Only single shot on single site testing is reported.

Table XI. Threshold for Bulk Laser Irradiation Induced Damage (DF laser light, $\lambda = 3.8$ μm)

Material	I_B(GW/cm^2)*	$R = I_B/I_B$(NaCl)
† MgF_2	18.5	1.19
CaF_2	25.5	1.65
SrF_2	28.5	1.84
BaF_2	27.5	1.77
† LiF	20.0	1.29
NaF	>30.0	>1.94
NaCl	15.5	1.00
Al_2O_3	25	1.61

* This table gives peak intensity on axis at the threshold for damage.
† These materials had nonuniform damage thresholds possible due to inclusions.

For the interest of the readers, we also include the ratio of damage thresholds for different materials normalized to that of NaCl. All the samples were obtained from commercial sources and were specified as having "high-power laser" finishes.

The measured bulk damage thresholds do not correlate with the total scattering which we measured. On the basis of visual observation we conclude that most of the scattering was caused by the inadequate

Table X. Scattering* in 2-5 μm Window Materials ($x10^3$)

Material	λ(μm) = 0.4762		0.6471		1.15		3.39	
	Forward	Backward	Forward	Backward	Forward	Backward	Forward	Backward
MgF_2	2.23	1.62	1.68	9.00	0.554	0.282	0.404	0.0807
CaF_2	3.64	4.54	2.15	2.36	0.960	0.541	0.532	0.0943
BaF_2	2.43		1.41	1.47	0.455		0.157	0.0658
SrF_2	1.98	2.68	1.16	1.39	0.404	0.318	0.179	0.0495
NaF	14.1	13.8	7.64	8.53	1.75	2.30	0.184	0.210
LiF	4.14		2.29	3.03	0.564		0.0973	0.0700

* Scattering is the fraction of the light scattered into the forward or backward 2π steradians with respect to the total quantity of light transmitted through the sample.

quality of the surface finishes. In fact, surface damage threshold for these samples was 5 to 10 times lower than the bulk damage threshold, and was determined by the low quality of the surface finishes. It is for this reason that we do not list the surface damage fluxes.

D. Summary of Pulsed Laser Damage Thresholds for Infrared Windows and Coatings

It is now possible to summarize the observed laser damage thresholds with numerical values that are generally accepted and which can serve as guides to the high power laser system designer. Table XII presents an overall summary of current data while Tables XIII, XIV, and XV give more detailed summaries for 10.6 μm transmissive materials, 2-5 μm transmissive materials and several coatings, respectively. Note that the data in Table XIII shows the strong sample to sample variability still found even in today's so-called best materials.

Table XII. Composite Summary of Pulse Laser Damage Thresholds in the Infrared

1. Alkali halides, bulk damage:

NaCl	~10 GW/cm^2	at 10.6 μm: Intrinsic
KCl	~7-8 GW/cm^2	at 10.6 μm: Intrinsic
NaF	~17 GW/cm^2	at 10.6 μm: Intrinsic

surface damage:

A. Generally ~1/5 to 1/10 of the bulk damage number.

B. For certain etched surfaces, can be as high as the bulk; however, etching sacrifices figure.

2. ZnSe bulk and surface damage at 10.6 μm occurs at ~0.4 GW/cm^2

3. Alkaline-earth fluorides, bulk damage:

CaF_2	~25 GW/cm^2	at DF wavelengths (~3.8 μm)
SrF_2	~28 GW/cm^2	at DF wavelengths (~3.8 μm)
BaF_2	~27 GW/cm^2	at DF wavelengths (~3.8 μm)

4. Sapphire (Al_2O_3) ~25 GW/cm^2 at 3.8 μm.

5. Coatings at 10.6 μm typically damage at ~0.4 GW/cm^2.

Table XIII. Pulse Laser Induced Damage Thresholds at 10.6 μm for IR Window Materials (Transparent at 10.6 μm) (Pulse duration ~100 nsec)

Material	On Axis Peak Power Density in GW/cm^2 Bulk Damage 1 on 1	Bulk Damage N on 1	Surface Damage 1 on 1	Surface Damage N on 1	Surface Finish	Possible Mechanism
Single Crystals:						
NaCl - conventional	9.83	9.89	1.6	1.9	Laser grade	Intrinsic - avalanche breakdown
NaCl - conventional	- -	- -	3.3	11.7	Etched	Surface defects - intrinsic
NaCl-RAP grown	< 0.38	< 0.38	- -	- -		Inclusions
KCl - conventional	6.1	7.1	1.6	4.9	Laser grade	Intrinsic - avalanche breakdown
KCl - RAP grown	< 0.38	< 0.38	- -	Shows		Inclusions
KCl - RAP grown	1.5	2.6	- -	sample to		Defects or inclusions
KCl - RAP grown	4.6	- -	0.46	sample	Conventional	Defects or inclusions
KCl - RAP grown	- -	> 7.8	3.0	*variations*	Etched	Intrinsic - avalanche breakdown
KBr - conventional	< 0.38	< 0.38	- -			Inclusions
KBr - RAP grown	7.23	15.35	- -			Intrinsic - avalanche breakdown?
NaF - conventional	16.49	17.07	- -			Intrinsic
Polycrystaline Press forged, doped:						
Press forged, RAP grown, KCl	- -	> 7.8	- -	2.7	Etched	Intrinsic
Press forged, Eu^{2+} doped KCl	1.91	1.91	0.93	1.39	Polish - etch polish	Defects or inclusions
CVD Prepared:						
ZnSe	0.46	0.46	0.35	0.35	Diamond polish	Inclusions

Table XIV. Pulse Laser Induced Damage Thresholds at 3.8 μm (DF laser) for IR Window Materials
(Transparent at 3.8 μm) (Pulse duration ~75 nsec)

Material	On Axis Peak Power Density in GW/cm^2 Bulk Damage 1 on 1	Bulk Damage N on 1	Surface Damage 1 on 1	Surface Damage N on 1	Possible Mechanism
Alkaline earth fluorides:					
MgF_2	18.5		To date all surface finishes on these materials were so poor that surface damage occurred at less than 1/10 the bulk threshold.		Inclusions
CaF_2	25.5				Inclusions - intrinsic?
SrF_2	28.5				Inclusions - intrinsic?
BaF_2	27.5				Inclusions - intrinsic?
Alkali-halides:					
LiF	20.0				Inclusion
NaF	>30.0				Intrinsic
NaCl	15.5				Intrinsic
Others:					
Al_2O_3	25				Inclusions - intrinsic?

Table XV. Pulse Laser Damage Threshold at 10.6 μm for Optical Coatings

Reflectivity	Coating Components	Substrate	Pulse Duration μsec	On Axis Peak Power Density, GW/cm^2
Dielectric enhanced maximum reflection	$ThF_4/ZnSe$	Ag-Mo	0.1	0.280
			1.0	0.305
			4.0	0.043
			6.0	0.034
Anti-reflection	CeF_3	KCl	0.1	0.35
	ZnS	KCl	0.1	0.40
	CeF_3/ZnS	KCl	0.1	0.14
- - -	ZnSe	KCl	0.1	0.58
Anti-reflection	$ZnSe/ThF_4/ZnSe$	KCl	0.1	0.47
	ZnSe/KCl/ZnSe	KCl	0.1	0.52

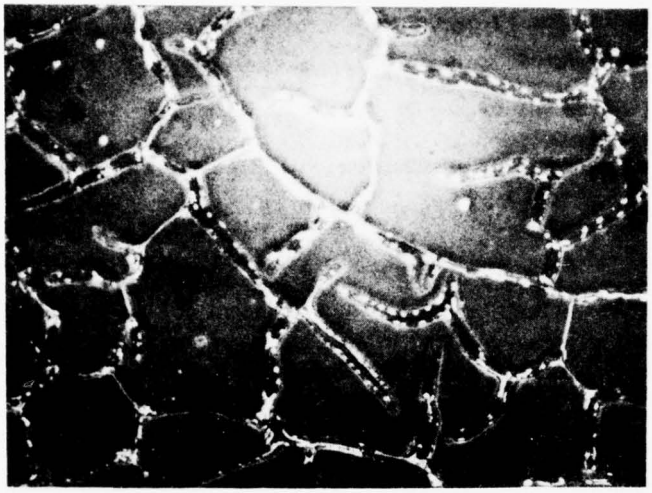
E. CW Damage to Optical Coatings - Comparison with Pulse Damage Thresholds

At the request of the HRL coatings group we tested several coatings to find CW laser damage thresholds. A 40 W, CW CO_2 laser was used. The TEM_{00} mode beam was focused with a 50 mm focal length lens to a spot having a 90 μm diameter (to the $1/e^2$ points in intensity). Thus, the maximum peak on-axis intensity we could develop was 1.3×10^6 W/cm^2. Each sample was exposed for 10 sec and the occurrence of damage was identified visually. The lased regions of the samples were inspected with light microscopy after irradiation.

Coating B109RF-2 (ZnSe/ThF/ZnSe) was badly crazed and damaged easily at 0.58 MW/cm^2. A very small area of sample 45-BF1 (ZnSe/ThF/ZnSe) could be damaged at maximum irradiation and B142B2 (ZnSe/KCl/ZnSe) and B11-10 (single ZnSe layer) showed no damage in our tests.

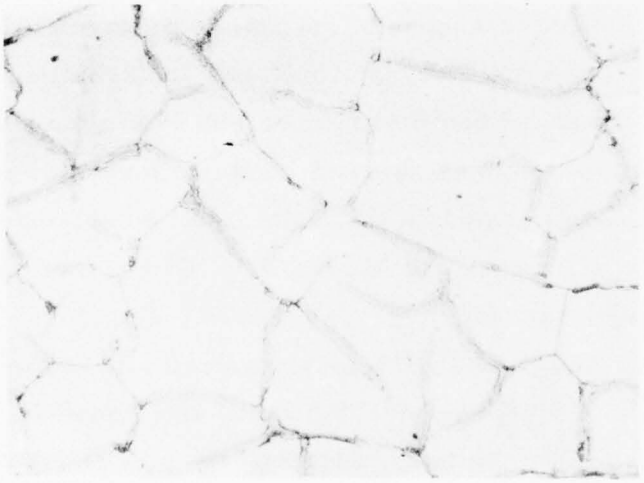
Figure 15 shows two micrographs of the ZnSe coating (B11-10). The crazing is on a different scale from that in Fig. 7 for a 3 layer AR coating. Also note that the phase contrast micrograph shows the presence of defects which do not appear with bright field illumination. It is possible that these defects which do not absorb in the visible (ie: do not appear with bright field illumination) may absorb in the infrared and thus contribute to the pulse damage mechanism.

Figure 16 shows a pulsed and a CW laser damage site on the same coating (B109RF2). Though this coating was badly crazed an examination of these sites is worthwhile. Both damage site diameters correspond closely to the focused laser beam diameter suggesting that they represent near threshold events. However, more of the coating has been removed in the CW case. The off center site within the pulsed laser damaged area is indicative of the role of defects in pulsed damage. For these sites, CW damage occurred with a 10.6 μm irradiance of 0.58 MW/cm^2 for 10 sec while pulse damage required ~500 MW/cm^2 for 10^{-7} sec.



PHASE CONTRAST
ILLUMINATION

100 μm



BRIGHT FIELD
ILLUMINATION

100 μm

Figure 15. Comparison of brightfield and phase contrast illumination micrographs. Crazing is present as well as defects which are not obvious in brightfield illumination.

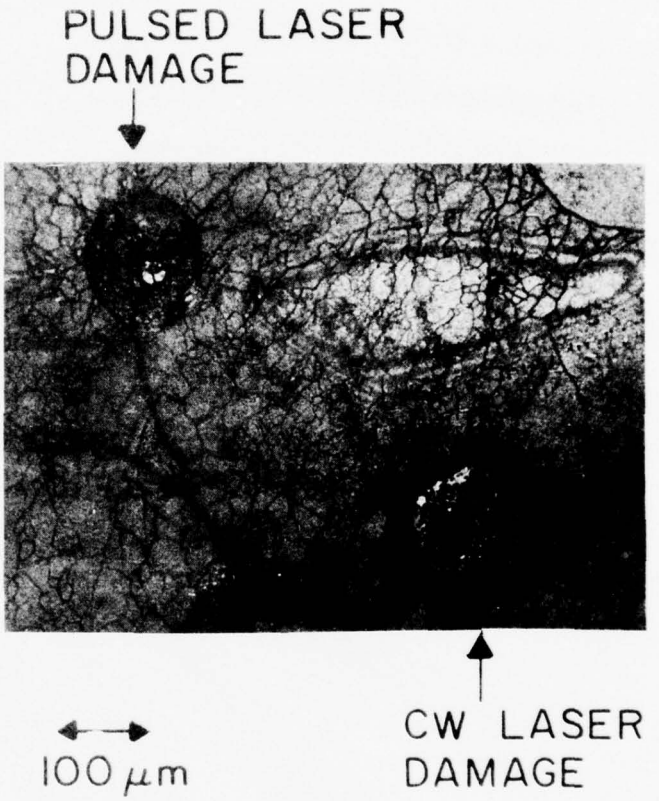
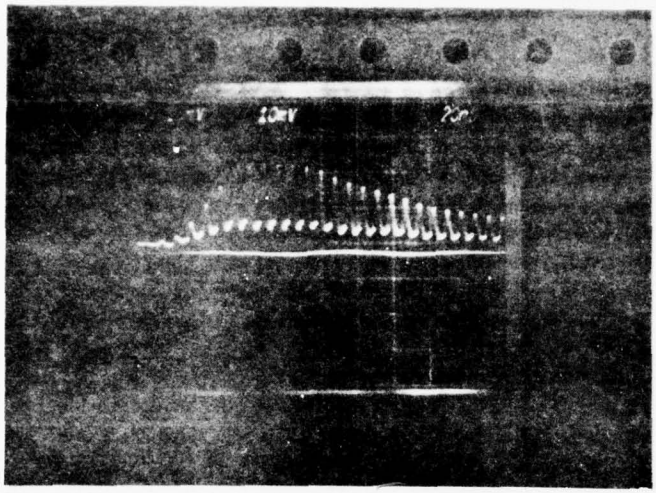


Figure 16. Pulsed and CW 10.6 μm laser damage to a ZnSe/ThF_4/ZnSe anti-reflection coating on KCl.

F. Data Acquisition System and Survival Curve Technique for Identifying Pulsed Laser Damage Mechanisms

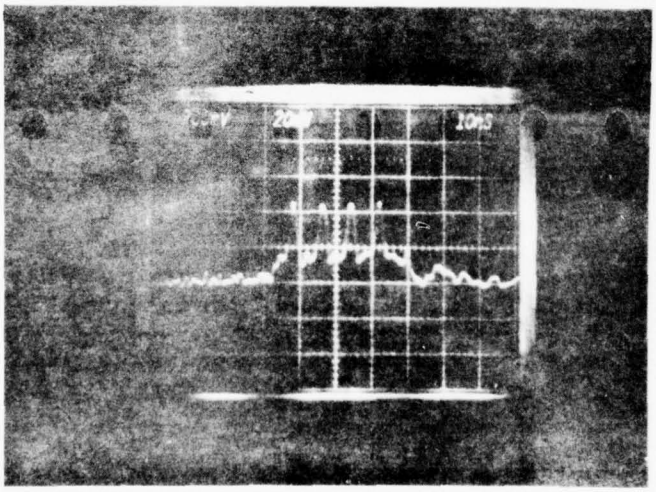
Because of the large quantity of data necessary for survival curve analyses of the laser damage mechanisms, a data acquisition system was requested for this program. Due to delays in funding, the data acquisition equipment was not ordered until late in the program. Therefore it did not arrive until mid-summer 1976. Our attempt to obtain identification of 10.6 μm damage mechanisms by using survival curve analyses will therefore occur in the future.

As evidenced by Fig. 17, the modulator and associated circuitry which we developed to obtain the necessary laser pulse waveform was operational during this program. One set of data, in the form of over 400 photographs such as the one shown in Fig. 18, was taken for survival curve analysis of ZnSe. This data was taken at one flux level and so can not give a complete idea of the damage process. When more data is available we shall analyze it all to try to identify the damage process.



20 NSEC / DIV

10.6 μm CO_2 TEA LASER OUTPUT WAVEFORM



10 NSEC / DIV

10.6 μm WAVEFORM AFTER CdTe MODULATOR SWITCH. FOR SURVIVAL CURVE STUDIES

Figure 17. Operation of the CdTe pulse modulator. Upper photo shows the input laser waveform. Lower photo shows the modulated waveform.

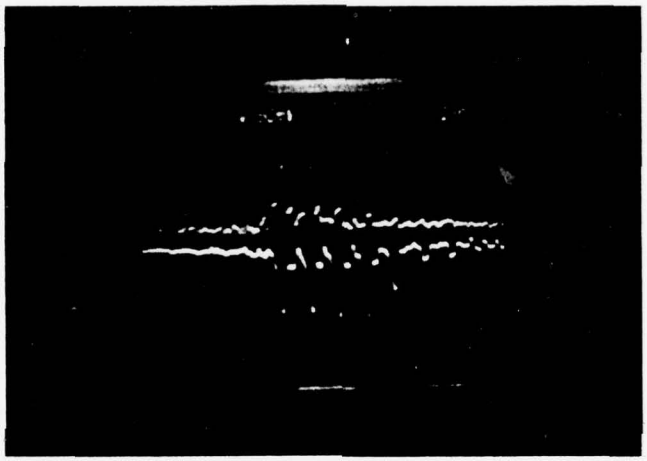


Figure 18. Oscilloscope photograph of transmitted (upper trace) and input (lower trace) pulse waveforms required for survival mechanisms. Sample was ZnSe.

IV. NON-CATASTROPHIC OPTICS DEGRADATION

(R. Joiner, C.P. Christensen, W.H. Steier, J.H. Marburger, M. Flannery)

A. Thermal Lensing

In an earlier report [18], we showed the results of far field intensity scans for an initially Gaussian 10.6 μm beam passing through a highly absorbing (β = 0.2 cm^{-1}) CdTe window. The experiment was carefully characterized in order to make a quantitative comparison with theory and computer predictions. The results were in good agreement.

B. Strain-optic Coefficient Measurements

In the same report, we presented an acousto-optic technique sometimes referred to as "The Dixon Method" for measuring strain-optic coefficients (P_{ij}) in window materials [19]. All three independent coefficients, P_{11}, P_{12}, P_{14}, were measured for both CdTe and GaAs at 10.6 μm. Theoretical values were available for GaAs, and a comparison showed good agreement for P_{11} and P_{14} but not in the case of P_{12}.

C. Strong Variations in Stress-Induced Birefringence in BaF_2 Due to Crystal Orientation

In an attempt to verify experimentally the theory of stress-induced birefringence for a ⟨111⟩ oriented crystal, it was discovered that the effect could be greatly enhanced or practically nulled, depending on the crystal orientation.

Figure 19 shows the experimental set-up. The stresses are created by a 25 W CO_2 laser passing through a 1 cm by 2 in. uncoated sample of BaF_2 (β = 0.2 cm^{-1} at 10.6 μm). A 4-inch diameter collimated linear polarized HeNe beam was used as the probe beam. The stress-induced cross-polarization was observed either visually on a screen or electronically by a scanner and PMT, after passing through a crossed analyzer polarizer. Figure 20 shows the typical cloverleaf

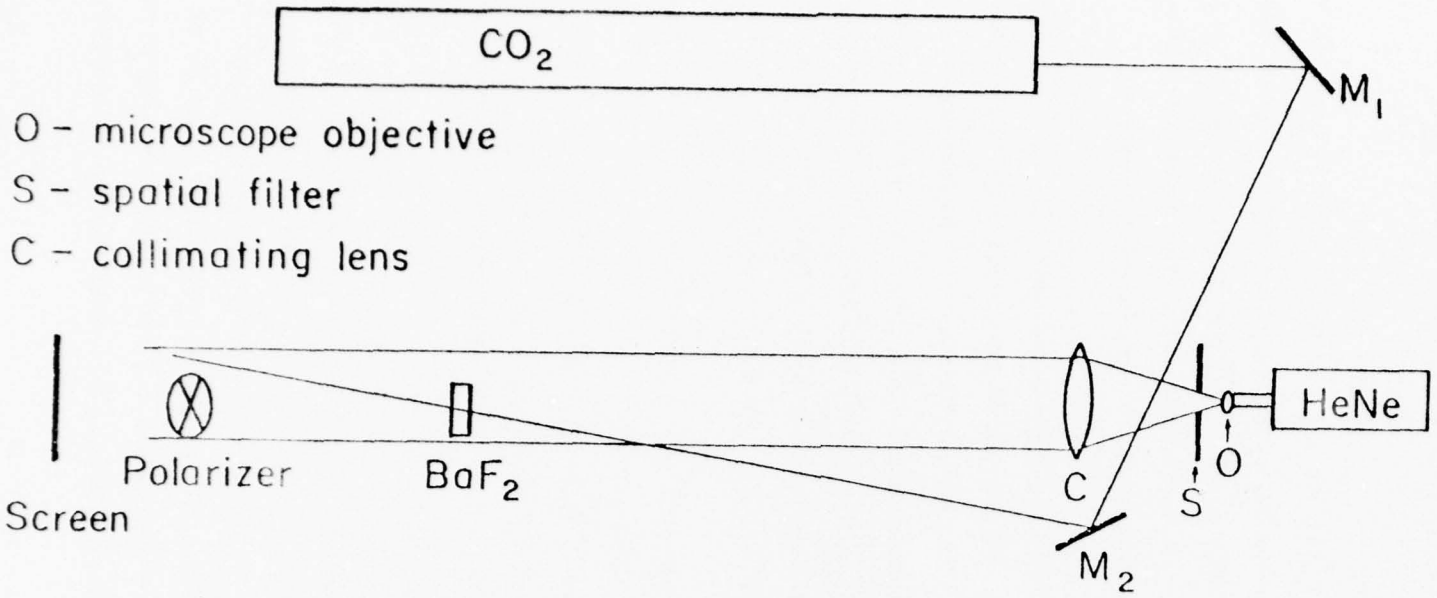


Figure 19. Schematic of experiment



Figure 20

Transmission pattern of cross polarization - normal incidence (⟨111⟩).

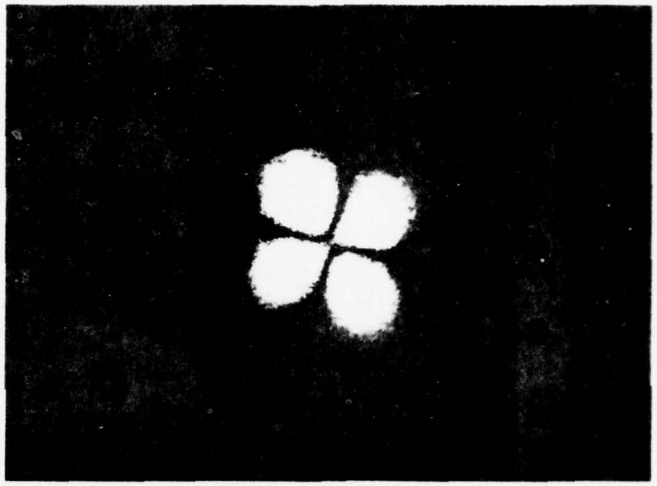


Figure 21

Transmission pattern of cross polarization - large angle incidence.

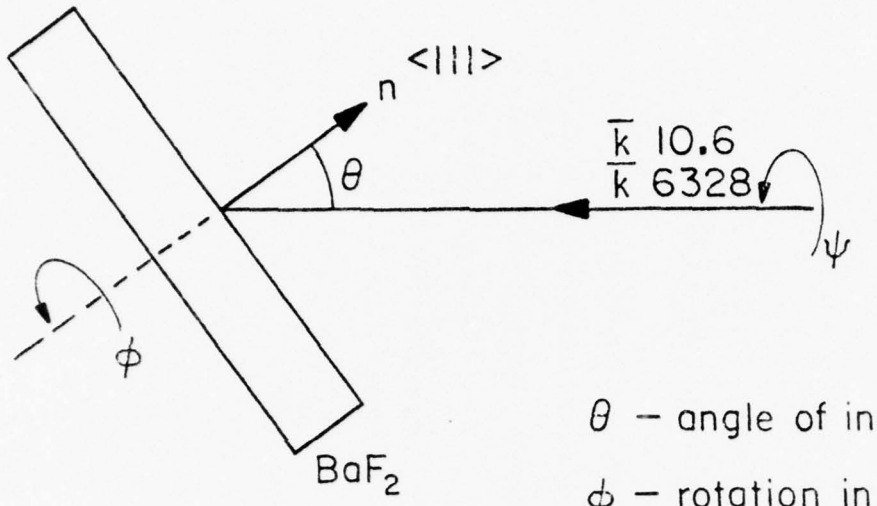
pattern after 10 to 15 seconds of heating. In the ⟨111⟩ plane, each point can be thought of as a waveplate with polarization eigenvectors in the radial and azimuthal directions with the center of the heating beam defining the origin of the cylindrical system. (A more complete description can be found in references [20] and [21]). Hence, the sin 2θ cloverleaf pattern simply results from varying components E_r and E_θ of the incident polarization E_x.

In an attempt to verify computer predictions with experimental scans of the pattern, it was found that the two could be made to agree simply by a small change in the angle of incidence. It was also discovered that a large change in angle of incidence (20^o-45^o) created an order of magnitude change in intensity and also rotated the cloverleaf pattern, Fig. 21.

In a second experiment, the crystal was rotated in the ⟨111⟩ plane for several different angles. The experiment of changing the angle of incidence was repeated in each case (see Fig. 22). In most cases the intensity increased and the pattern rotated by the different amounts. However, in one particular case, as the angle of incidence was increased, the intensity decreased almost to a null, then increased in intensity again.

The last experiment was to set the angle of incidence to this null and rotate the sample in the plane of the sample (⟨111⟩). Three nulls were discovered, 120^o apart, as would be expected, since the ⟨111⟩ direction is a threefold symmetry axis. The pattern was also observed to rotate with the rotation of the sample.

A theoretical investigation of the observed phenomena is nearly complete. Since BaF_2 is elastically almost isotropic ($S_{44}/2(S_{11}-S_{12}) = 0.98$), the solution of the stress-strain problem for the ⟨111⟩ case is valid for all crystal directions. The high degree of anisotrophy is found in the fourth rank π tensor relating stress to index change. An expression for



θ – angle of incidence

φ – rotation in plane of crystal about <111>

ψ – angle about direction of beam propagation

θ, φ, ψ – Euler angles

Figure 22. Euler angles describing tilt and rotations of BaF_2 sample

the cross-polarization term is given by

$$E_y(L) = je^{j\nu} \sin\left(\frac{k}{2} n^3 L \sqrt{(\Delta B_{rr} - \Delta B_{\psi\psi})^2 + (2\Delta B_{r\psi})^2}\right) \times \frac{[(\Delta B_{rr} - \Delta B_{\psi\psi}) \sin 2\psi + (2\Delta B_{r\psi}) \cos 2\psi] E_x(0)}{\sqrt{(\Delta B_{rr} - \Delta B_{\psi\psi})^2 + (2\Delta B_{r\psi})^2}} \quad (1)$$

where $\Delta B = -2 \frac{\Delta n}{n^3} = \pi\sigma$.

In the $\langle 111 \rangle$ plane, the cross term $\Delta B_{r\psi}$ is equal to zero and Equation 1 simplifies to

$$E_y(L) = je^{j\nu} \sin (k/2\, n^3 L\, (\Delta B_{rr} - \Delta B_{\psi\psi})) \sin 2\psi.$$

The presence of a non-zero cross term explains the rotation of the pattern. The new π_{ij}'s will be a linear combination of all the old π_{ij}'s in the $\langle 111 \rangle$ system. In that system, only π''_{41} and π''_{51} had any angular dependence. Derivatives with respect to angle give $\cos 3\phi$ and $\sin 3\phi$ which is consistent with the nulls being 120° apart.

The existence of special window orientations in which the cross polarized components of the exit beam polarization nearly vanishes suggests that the deleterious effects of strain-induced birefringence can be diminished by appropriate choice of crystal orientation and beam polarization. This point is discussed further in section IV. D.

IV. D. Theory of Thermally Induced Birefringence in Polycrystalline Media

During this contract, we have developed a theory of stress-induced birefringence in polycrystalline media when the individual crystal size is much less than a wavelength. This theory, which is described in references [22] and [23], gives expressions for the two independent elements P^*_{11} and P^*_{12} of the effective isotropic strain optic tensor P^*_{ij} when the single crystal has cubic symmetry. Using these expressions, we computed the birefringence induced in a window by a circularly symmetric incident beam. That is, we computed the phase difference introduced locally between the radial and azimuthal polarization components of the incident beam as it propagates through the window. The magnitude of this phase difference is proportional to a material parameter (called F/A in reference [24]) involving the elastic and piezo elastic tensor elements of the window material. We found that previous estimates of this parameter obtained by inserting the crystalline values of P_{11} and P_{12} into the expression appropriate for an isotropic medium predict roughly the correct order of magnitude but frequently the wrong sign. Of greater interest is a comparison between the correct polycrystalline result and the exact result for a single crystal window with ⟨111⟩ orientation [24]. This comparison showed that birefringence effects are reduced by about one order of magnitude in going from the ⟨111⟩ single crystal case to the ideal polycrystalline case.

The important question next to be resolved is, can a non-ideal polycrystal reduce the birefringence effects even further? We are encouraged in thinking so by two facts, one theoretical and one experimental. The theoretical point is that the sign of $P_{11}-P_{12}$ is opposite that of $P^*_{11}-P^*_{12}$ for the important IR window materials KCl, KBr, CaF_2 and BaF_2. By orienting the grains of a polycrystal preferentially along some axis (not a 111 axis) it may be possible to reduce the magnitude of

$\overline{P}_{11}-\overline{P}_{12}$, where $\overline{P}_{ij}$ plays the role in the partially oriented polycrystal that P^*_{ij} does in the ideal polycrystal. We have been trying to carry through a computation of $\overline{P}_{ij}$ for a partially oriented polycrystal, but have not been able to make much progress. In order to obtain analytically tractable starting equations it looks as if it will be necessary to put up with a theory less accurate than that which was used for computing P^*_{ij} for the ideal polycrystal.

The encouraging experimental fact is the observation, described in section IV. C, that birefringence effects in a ⟨111⟩ single crystal window are diminished in off-axis propagation of a plane polarized incident beam. This suggests that a single window aligned in some plane other than ⟨111⟩ will have reduced birefringence effects for a certain polarization direction of the incident beam. One would expect a polycrystalline window to exhibit reduced thermal birefringence if its grains possessed a mean orientation in the direction corresponding to the single crystal window orientation which gives minimum birefringence.

We are struggling to make these speculations quantitative. The theory of non-ideal polycrystals, however, is in a primitive state of development, and it is likely that only experiments relating polycrystal texture to induced birefringence can give credible indications of the feasibility of this birefringence reduction scheme.

V. CONCLUSIONS

The conclusions of the work described in this report are presented below where they are categorized as is the work in the text:

A. Defects in ZnSe

High temperature measurements of the Hall effect and the conductivity of single crystals of ZnSe doped with a donor (Al) or an acceptor (As) showed the electron concentrations to be proportional to the square root of zinc pressure, donor concentration, and inverse acceptor concentration. The electron concentration of constant zinc pressure and doping concentration increased with increasing temperature in donor-doped samples, but decreased with increasing temperature in acceptor doped samples. Through a combination of the present results with those of other workers, a defect model can be developed which is governed by ionic defects due to ionized dopants and native defects such as V''_{Zn} and $V^{\bullet\bullet}_{O}$ or $Zn^{\bullet\bullet}_{i}$. We also determined the parameters of the ionic disorder constants K''_{S} or K''_{F}. However, experiments on gallium doped ZnSe failed to explain the observed promotion of hole conduction by incorporation of gallium. This dopant is usually believed to be a donor.

Annealing Ga-doped ZnSe (100 ppm Ga) at 700°C under various Zn-partial pressures in the range of 10^{-3} to 10^{-1} atmos. was found to induce noticeable changes in the defect substructure. On increasing the partial pressure, at $P_{Zn} \sim 3 \times 10^{-2}$ the microstructure revealed the formation of a moderately high density of unfaulted prismatic loops lying on the ⟨110⟩ and ⟨111⟩ planes. These loops have been identified by image contrast analyses to be due to the condensation of excess Zn and also by Se vacancies. At still higher Zn-partial pressures the loop concentration decreased drastically and only the presence of some unidentified precipitate was observed. Preliminary analysis shows that some correlation exists between the annealing induced changes in the carrier

concentration of this sample and the changes in defect structure observed in the electron microscope.

B. Pulsed Laser Induced Damage

Our results indicate that the damage threshold depends on the manner of irradiation as shown by the N on 1 and 1 on 1 experiments. This effect appears to be caused by the presence of inclusions or defects in the materials. When inclusions or defects are present the damage threshold is dependent upon the particular sample studied and the volume of the site irradiated. A thorough study of a material must necessarily include measurements of several samples. Various focal spot sizes should be used with the intrinsic breakdown limit being approached for very small spot sizes.

Pulse laser damage at 10.6 μm to three layer A-R films on KCl substrates occurs at ~450 MW/cm^2 and appears to be determined by inclusions or defects. When these films were exposed to a focused CW 10.6 μm catastrophic failure occurred at ~1 MW/cm^2 in some areas. However, most of the films we tested could withstand a flux of 1.3 MW/cm^2 for 10 sec.

The alkaline-earth fluorides tested in this work have very similar bulk damage thresholds (~25 GW/cm^2 at 3.8 μm) and the site morphology suggests that inclusions or defects were responsible for the damaging interaction. The surface damage thresholds for these samples were much lower than the bulk damage thresholds. This can be attributed to poor surface finish quality and leads us to recommend that improved polishing techniques be developed in order to make these materials applicable to high power laser systems.

We also found that sapphire has a very high bulk damage threshold, 25 GW/cm^2 at 3.8 μm. Since sapphire is mechanically strong and readily available in large pieces, it should be considered for use in the 2-5 μm region.

C. Non Catastrophic Optics Failure

The theory of thermal lensing without birefringence effects appears to predict accurately and quantitatively the experimental results observed at 10.6 μm. The measured strain-optic coefficients of CdTe and GaAs at 10.6 μm agree well with the theory in the case of P_{11} and P_{14} but show a large disagreement for P_{12}. We found the stress-induced birefringence in certain window materials to be a strong function of the direction of propagation through the crystal, and the effect can be minimized with the proper choice of direction. This would indicate a preferred orientation for the crystallites in polycrystalline-forged materials and that polycrystals can be designed in which stress-induced birefringence is significantly reduced over single crystals.

VI. RECOMMENDATIONS

As a result of the work described in this report, we may make the following recommendations:

1. The lumonics HF/DF pulsed laser cavity should be upgraded with a properly designed resonator and the damage measurements at 3.8 μm should be checked. Measurements at 2.8 μm should be taken.

2. Techniques for damage resistant surface finishing of 2-5 μm optical materials should be developed.

3. The studies of laser damage mechanisms using the survival curve technique should be completed.

4. Damage thresholds for 10.6 μm optical coatings should be determined and, if possible, the survival curve technique used to identify the damage mechanism.

5. The implications of the difference between thresholds measured using different irradiation sequences should be explored.

6. Theoretical analyses concerning the design of stress-induced birefringence-free polycrystalline materials should be carried out.

REFERENCES

1. P.B. Hirsch, A. Howie, R.B. Nicholson, D.W. Pashley, and M.J. Whelan, Electron Microscopy of Thin Crystals (Butterworth, London, 1965).

2. F.A. Kroger and A.K. Ray, This report, section II.

3. G.H. Narayanan and A.H. Kacharie, Phys. Stat. Sol. 26 A, 657 (1974).

4. B. Hughes and G.H. Narayanan, unpublished.

5. M. Bass and K.M. Leung, IEEE J. Quant. Electron. QE-12, 82 (1976).

6. S.D. Allen, M. Braunstein, C. Giuliano and V. Wang, NBS Special Publication No. 414, 66 (1974).

7. E. Yablonovitch, Appl. Phys. Lett. 19, 495 (1971).

8. K.M. Leung, M. Bass and A.G.J. Balbin-Villaverde, NBS Special Publication No. 435, 107 (1975).

9. D.W. Fradin, E. Yablonovitch and M. Bass, Appl. Optics 12, 700 (1973).

10. L.G. DeShazer, B.E. Newnam and K.M. Leung, NBS Special Publication No. 387, 114 (1973).

11. M. Braunstein, D. Zuccaro, J.E. Rudisill and A. Braunstein, "Low Absorption Antireflection Coatings for KCl," Proceedings 5th Annual Conference on Infrared Laser Window Materials, Las Vegas, Nevada, 1-4 December, 1975.

12. C.C. Tang, K.M. Leung and M. Bass, "Re-examination of Laser Induced Breakdown in the Alkali Halides at 10.6 μm," presented at the 1976 Symposium on Optical Materials for High Powered Lasers, Boulder, Colorado, 13-15 July, 1976.

13. V. Wang. C.R. Giuliano and B. Garcia, "Single and Multilongitudinal Mode Damage in Multilayer Reflectors at 10.6 μm as a Function of Spot Size and Pulse Duration," NBS Special Publication No. 435, 216 (July 1975).

14. A.E. Siegman, Proc. IEEE 53, 277 (1965).

15. For example, see P.A. Temple and M.J. Soileau, "Resonant Defects Enhancement of the Laser Electric Field," Proc. 1976 Symposium on Optical Materials for High Powered Lasers, Boulder, Colo., July 1976.

16. M. Hass, J.A. Harrington, D.A. Gregory and J.W. Davisson, Appl. Phys. Lett. 28, 160 (1976).

17. J.A. Harrington, D.A. Gregory and W. Ott, "Infrared Absorption in Chemical Laser Window Materials," Appl. Opt. (to be published).

18. C. Christensen, W.H. Steier, and R. Joiner, Proceedings of the Fifth Annual Conference on IR Laser Window Materials, December, 1975, p. 469.

19. R. Joiner, W.H. Steier, C. Christensen, Proceedings of the Fifth Annual Conference on IR Laser Window Materials, December, 1975, p. 937.

20. J. Marburger, M. Flannery, University of Southern California "IR Window Studies," Quarterly Technical Report No. 6 (December, 1973) AFCRL, Contract No. F 19628-72-C-0275, ARPA Order No. 2055, p. 61.

21. B. Bendow, P.D. Gianino, M. Flannery and J. Marburger, Proceedings of the Fourth Annual Conference on IR Laser Window Materials, November 1974, p. 300.

22. M. Flannery, J. Marburger, Proceedings of the Fifth Annual Conference on IR Laser Window Materials, eds. C.R. Andrews and C.L. Strecher, Feb. 1976.

23. M. Flannery and J. Marburger, Appl. Phys. Lett. 28, 600 (1976).

24. M. Flannery and J. Marburger, University of Southern California "IR Window Studies," Semi-annual Technical Report No. 1 (31 March 1976) AFCRL Contract No. F 19628-76-C-0162, ARPA Order No. 2055.

BIBLIOGRAPHY

The following papers were presented or published as a result of the research described in this report:

1. Bass, M. and Leung, K.M., IEEE J. Quantum Electron. QE-12, 82 (1976); also presented at Fifth Conference on IR Laser Window Materials, Dec. 1975.

2. Bass, M., Leung, K.M., Tang, C.C. and Soileau, M.J., "Pulsed Laser Induced Damage at the DF Laser Wavelength," 1976 Symposium on Optical Materials for High Powered Lasers, Boulder, Colo., July 1976; also presented at CLEOS, San Diego, Calif., May 1976.

3. Christensen, C., Steier, W.H. and Joiner, R., "A Quantitative Experimental Investigation of Thermal Lensing," Fifth Annual Conference on IR Laser Window Materials, Dec. 1975.

4. Flannery, M. and Marburger, J.H., Appl. Phys. Lett. 28, 600 (1976).

5. Joiner, R., Steier, W.H. and Christensen, C., "Measurement of Strain-optic Coefficients by Acousto-optic Interactions," Fifth Annual Conference on IR Laser Window Materials, Dec. 1975.

6. Narayanan, G.H. and Rustomji, S.H., "The Microstructure of CdTe as Influenced by Thin Foil Artefacts", (to be submitted to Phys. Stat. Solid).

7. Rockwell, D.A. and Parks, J.H., J. Appl. Phys. 47, 4405 (1976).

8. Rustomji, S.H. and Narayanan, G.H., "A Transmission Electron Microscope Study of Annealing-Induced Defects in P-doped CdTe (in preparation).

9. Swaminathan, V. and Copley, S.M., J. Appl. Phys. 47, 4405 (1976).

10. Tang, C.C., Leung, K.M. and Bass, M., "Re-examination of Laser Induced Breakdown in the Alkali Halides at 10.6 μm," 1976 Symposium on Optical Materials for High Powered Lasers, Boulder, Colo., July 1976.

11. Zuccaro, D., Braunstein, M., Bass, M., Leung, K.M. and Tang, C.C., "Status Report of Three Layer 10.6 μm AR Coatings on KCl", 1976 Symposium on Optical Materials for High Powered Lasers, Boulder, Colo., July 1976; also at CLEOS, San Diego, Calif., May 1976.

APPENDIX A

Vibrational Modes of Defects in $Zn_xCd_{1-x}Te:P$ and $Mg_xCd_{1-x}Te:P$

B.V. Dutt and W.G. Spitzer

Departments of Materials Science and Physics

University of Southern California, Los Angeles, California 90007

Abstract

Infrared absorption measurements of phosphorus defects in $Zn_xCd_{1-x}Te:P$ and $Mg_xCd_{1-x}Te:P$ are reported. The localized vibrational modes of (Zn-P) and (Mg-P) pairs suggest a difference in pairing behavior of Zn and Mg with two P-centers previously noticed in CdTe:P. Magnesium primarily pairs with a neutral phosphorus complex, while zinc pairs with a phosphorus substitutional on Te-sublattice, a shallow acceptor.

A recent study gave an account of the infrared absorption attributed to the localized vibrational modes of phosphorus in CdTe[1]. Three absorption bands related to P vibrational modes were observed. Their peaks occur at frequencies of 269, 308 and 322 cm^{-1} at 80°K. Hereafter, these bands are referred to as A_1, A_2 and B respectively. It was tentatively proposed that the three bands arise from two different phosphorus defect centers. The band, B, was tentatively assigned to the vibrational modes associated with phosphorus substitutional on the Te-sublattice, P_{Te}, which is a shallow acceptor. Both the A_1 and A_2 bands were proposed to arise from a neutral phosphorus complex with axial symmetry. These assignments were based on the behavior of the bands with variation of the P concentration, [P] and the pairing effect of group III donor impurities In and Ga with P in double-doped CdTe.

In the present study, the absorption measurements are extended to include the P-doped mixed crystal systems, $Zn_xCd_{1-x}Te$:P and $Mg_xCd_{1-x}Te$:P. The principal objective is to provide a clearer identification of the P-defects in CdTe than was previously possible. The results are discussed in this vein to determine if they are consistent with the prior tentative assignments for the P-bands.

The ZnTe and MgTe are known to form binary alloys with CdTe. The lattice vibrational spectra of both $Zn_xCd_{1-x}Te$ and $Mg_xCd_{1-x}Te$ show the "two-mode" type of behavior in the reststrahlen region[2,3]. For small values of x the Zn produces a mode near $\nu \approx 166\ cm^{-1}$ at room temperature[2]. Since the zone center optical mode frequencies for CdTe are $\nu_{LO} \approx 170\ cm^{-1}$ and $\nu_{TO} \approx 141\ cm^{-1}$, the Zn-mode is an in-band resonance, and it is well removed from the frequency range where the P-related modes occur in CdTe.

The Mg is a light impurity in CdTe and at small x it gives rise to one localized vibrational mode for each of the three principal Mg isotopes. The frequencies are in the vicinity of 250 cm^{-1} close to the P-related bands.

The range of composition of the mixed crystals $Zn_xCd_{1-x}Te$:P and $Mg_xCd_{1-x}Te$:P studied here was limited to $x \lesssim 0.20$ (4×10^{21} cm^{-3}) for Zn and $\lesssim 0.05$ (1×10^{21} cm^{-3}) for Mg while the [P] $\lesssim 5 \times 10^{19}$ cm^{-3}. The crystal growth was by the horizonal Bridgman method and the technique was similar to that described previously[1]. The starting materials were 6N purity Cd,Te, Zn or Mg in the desired stoichiometric ratio. The P was added in elemental form or in the form of Cd_3P_2. In all cases, the ingots were well-compensated in the as-grown state. The impurity concentrations given here are not well established as they are estimated from the amounts added to the melt and the available segregation coefficient information.[1] However, the observations made here require only comparisons of the relative doping levels and in many cases only order of magnitude values are of significance. In the Figs. 1 to 4, it will also be noticed that the doping efficiency of P is improved in the mixed alloys for $x > 0$, than in CdTe. This is probably due to the reduced activity of P in the presence of Mg or Zn. Therefore, determination of precise impurity concentrations was not found to be essential for the discussions presented here. The optical data were obtained from differential transmission measurements at 80°K from ν = 220 to 390 cm^{-1} which encompasses the infrared region in which the P-related localized vibrational mode absorption bands occur. In all cases, an undoped low absorption CdTe crystal of thickness, d, equal to that of the doped sample was used as reference. The absorption coefficient was obtained from the measured differential transmission, $T_{diff} = e^{-\alpha d}$ for all samples, assuming the difference in

reflectivity between the sample and the reference as negligible.

(A) $Zn_xCd_{1-x}Te$:P

Figure 1 shows the absorption spectra of a series of $Zn_xCd_{1-x}Te$:P samples, where [P] is kept constant at ~ 5×10^{19} cm^{-3} and x is varied from 0 to 0.20. As [Zn] is increased, several new bands appear in addition to the P-bands A_1, A_2 and B present in x = 0 sample. Two major features are the growth of the A_2-band at 308cm^{-1} and the appearance of a band near 343cm^{-1}. The strong B-band of P_{Te} decreases with increasing x and has disappeared by x = 0.20, while the A_1-band is present at all x, although greatly broadened. The band near 332 cm^{-1} appears in samples with x > 0, but is not observed at x = 0.05. The band at 317 cm^{-1} appears in the x = 0.015 sample, is far more intense at x = 0.05 but then decreases with increasing x and has disappeared at x = 0.20. All of the frequencies indicated above are meant only to identify the bands and are only approximate as all the bands including A_1, A_2 and B show some shift to higher frequency as x increases. All of the bands including the new ones are P-related. This is demonstrated in Fig. 2 where the strengths of all bands decrease when [P] is reduced for a fixed x = 0.05.

A simple interpretation can be given for most of the major features of the absorption spectra of Fig. 1. As the [Zn] is increased, purely on the basis of a random distribution of [Zn], the probability of finding a P_{Te} with no Zn_{Cd} as nearest neighbor would be $\propto(1-x)^4$. Thus as x is increased with [P] held constant the B-band of P_{Te} would be expected to decrease in intensity. However if there is preferential pairing of Zn_{Cd} with P_{Te}, the B-band should decrease even

more rapidly. Thus the reduced strength of this band with increasing x and its absence at x = 0.20 is apparently due to the preferential formation of Zn_{Cd}-P_{Te} pairs. A P_{Te} with three Cd_{Cd} and one Zn_{Cd} nearest neighbors reduces the P-defect symmetry from T_d to axial C_{3v}. Since the isolated Zn_{Cd} causes a much lower frequency resonance mode, an approximate description of the effect of a Zn_{Cd} next to a P_{Te} would be to split the triply degenerate band of the P_{Te} (T_d) defect into two bands, one from the doubly degenerate modes transverse to the pair axis and one from an axial mode. This behavior has been observed in a number of similar cases in other systems[4]. Two new Zn_{Cd}-P_{Te} pair bands are therefore expected and they can account for both the band near 343 cm^{-1} and the growth of the A_2-band at 308cm^{-1}. In all of the samples of Fig. 1, the integrated absorption of $\int \alpha d\nu = \int \alpha d\nu + \int \alpha d\nu$ indicating that the 308cm^{-1} band is the superposition of two bands, one being the original A_2-band of the P-complex and the other being one of the two Zn_{Cd}-P_{Te} bands. It is of interest to note that the A_1 and the A_2 part of the 308cm^{-1} band both persist to x = 0.20 indicating the stability of the P-complex. The absence of new split bands in the vicinity of A_1 and A_2 suggests that the Zn_{Cd} does not show preferential pairing with that part of the phosphorus present in the complex. This is particularly noteworthy since with random statistics and $X \geq 0.1$ such bands should be visible if they are present. The A_1-band at 269 cm^{-1} is inhomogeneous line broadened since there may be many different weakly interacting positions for Zn near a P-complex. An explanation of the behavior of the weak 332 cm^{-1} and 317 cm^{-1} bands as well as the 297 cm^{-1} band which is present only in the x = 0.2 sample requires a more detailed model than that used here. However, the present results do appear to be consistent with the previous interpretations of

the P-related bands in CdTe.

(B) $Mg_xCd_{1-x}Te:P$

Figure 3 gives the absorption spectra of a series of $Mg_xCd_{1-x}Te:P$ samples with a constant [P] $\approx 5 \times 10^{19}$ cm^{-3} and $0 \leq x \leq 0.05$. Fig. 4 shows the results for a constant $x = 5 \times 10^{-4}$ ($\sim 10^{19}$ cm^{-3}) and [P] $\sim 5 \times 10^{19}$ and 2×10^{17} cm^{-3}. There is a good deal of structure observed. The three bands near 244, 248 and 252 cm^{-1} are those due to the localized vibrational modes of $^{26}Mg_{Cd}$, $^{25}Mg_{Cd}$ and $^{24}Mg_{Cd}$. Each of these is a T_d defect and the modes are triply degenerate. These modes have been reported previously[2] and it is apparent from Fig. 4 that they are independent of [P] for a given [Mg] and therefore unrelated to P. They will not be considered further. The principal observations in the present case are (a) the development of two new absorption bands at 278 and 343 cm^{-1}, each with a shoulder, (b) the reduced intensity of the A_1 and A_2 bands of the P-complex and (c) no significant change in intensity of the B-band of P_{Te} at 322 cm^{-1}. Some of the minor features observed in Figs. 3 and 4 will not be considered here.

A comparison of the spectra of Figs. 3 and 4 with the corresponding spectra of $Zn_xCd_{1-x}Te:P$ of Figs. 1 and 2 suggests that the system $Mg_xCd_{1-x}Te:P$ shows a different behavior from that of the $Zn_xCd_{1-x}Te:P$. Since there is no major change in intensity of the B-band of isolated P_{Te} in the alloys while the A_1 and A_2 bands of the P-complex decrease in intensity and vanish at $x = 0.05$ and there is the simultaneous development of the new major bands at 278 and 343cm^{-1}, it is clear that Mg_{Cd} is interacting primarily with the P-complex. This behavior is in

contrast to that of Zn_{Cd} in which the only detectable pairing is with P_{Te}. The degree of interaction of Mg_{Cd} with P_{Te} is not clear from the data. It is possible that the shoulders observed on the 278 and 343cm^{-1} bands might be related to the formation of Mg_{Cd}-P_{Te} pairs. Thus it appears that Zn does not interact with the P-complex, but pairs with P_{Te}. On the other hand, Mg interacts with the P-complex and its pairing with P_{Te} is uncertain, but probably less than similar pairing in the $Zn_xCd_{1-x}Te$:P case. The absence of A_1 and A_2 bands in the $Mg_xCd_{1-x}Te$:P sample with $x = 0.05$ and their nearly equal strength in the other samples is also consistent with the interpretation that these two bands are from a single P-complex in CdTe.

It is interesting to note that Mg and Zn, both isoelectronic with Cd, pair differently with P in CdTe. This may be related to the fact that the phosphorus compounds of Mg and Zn have different structures[5]. Mg_3P_2 forms with tetrahedral coordination while Zn_3P_2 has tetragonal form. In addition, MgTe is hexagonal while ZnTe is tetrahedral. A clue to the identity of the P-complex responsible for the A_1, A_2 bands lies in correlating these differences and finding a complex which permits pairing of Mg and P with tetrahedral coordination. In order to explain the Hall data of CdTe:P, a number of defects including some P-complexes were recently advanced[6]. One of the complexes is $(P_{Cd}\text{-}P_i)^x$ and it is attractive in that it satisfies the conditions of electrical neutrality and it allows tetrahedral coordination with Mg. However, further experiments are needed before any definite conclusions can be reached.

REFERENCES

1) B. V. Dutt and W. G. Spitzer, J. Appl. Phys. (to be published). (Ms #1453 R)

2) H. Harada and S. Narita, J. Phys. Soc. of Japan, 30, 1628 (1971).

3) S. Nakashima, T. Fukumoto, A. Mitsuishi and K. Itoh, J. Phys. Soc. of Japan, 35, 1437 (1973).

4) R. C. Newman, Infrared Studies of Crystal Defects (Barnes and Noble Books, New York, 1973).

5) R. W. G. Wyckoff, Crystal Structures, 2nd ed. (J. Wiley and Sons, New York, N.Y., 1963), Vols. 1 and 2.

6) F. A. Selim and F. A. Kröger, J. Electrochem. Soc. (to be published).

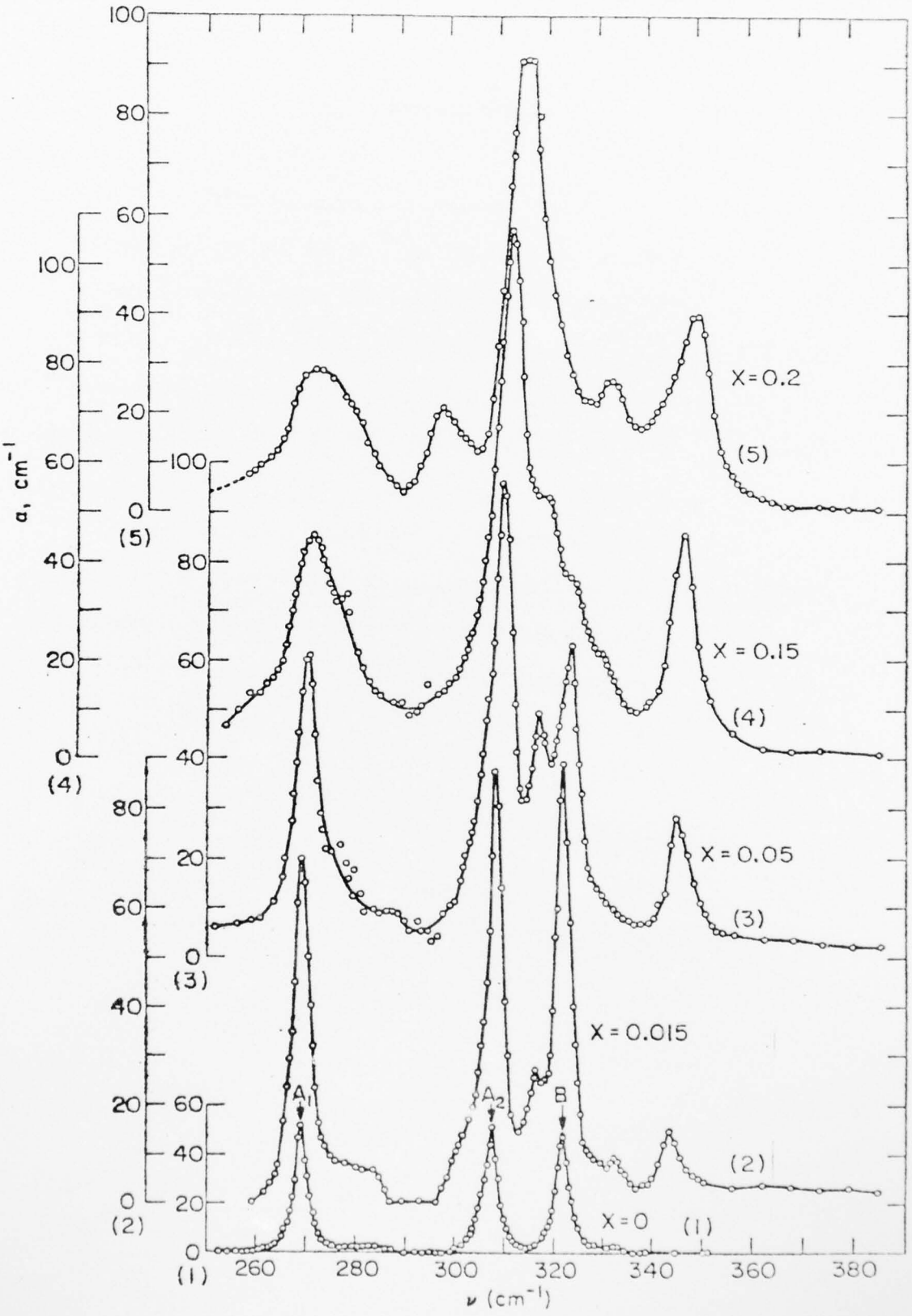
FIGURE CAPTIONS

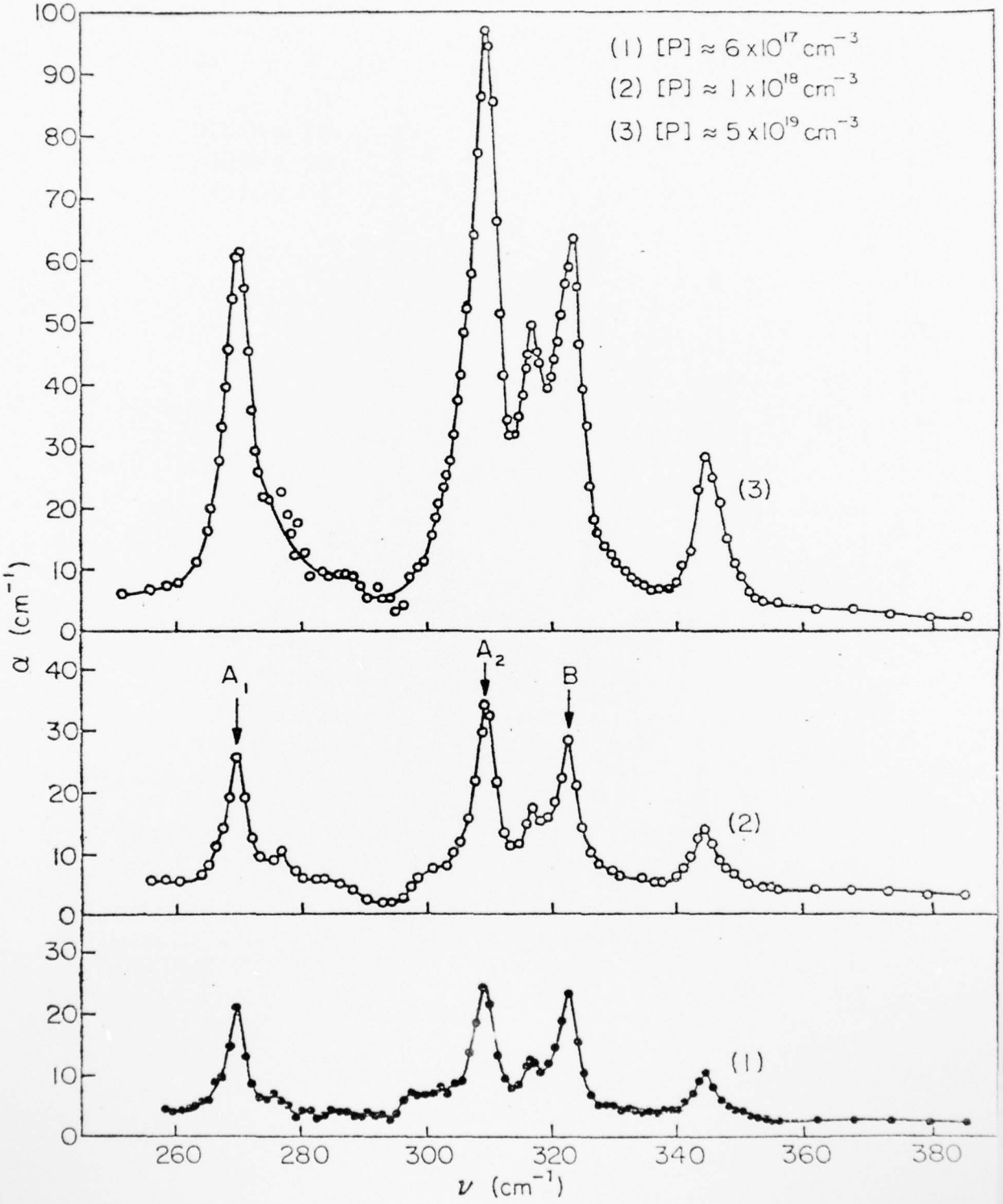
Figure 1 $Zn_xCd_{1-x}Te$:P Absorption spectra at 80°K. x is varied keeping [P] $\approx 5 \times 10^{19} cm^{-3}$ in all (1) to (5) samples. The scale numbers correspond to the curve numbers.

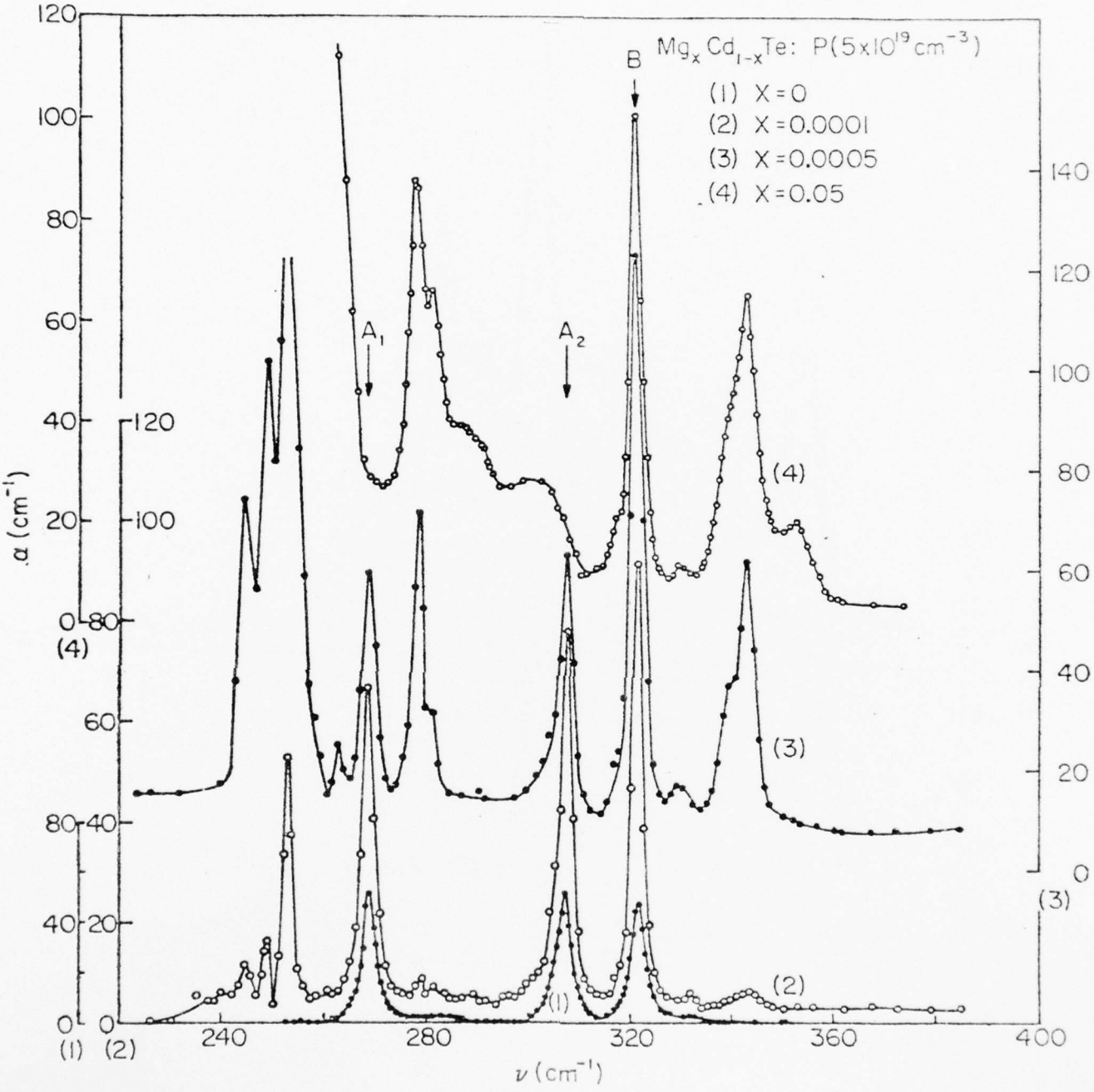
Figure 2 $Zn_xCd_{1-x}Te$:P Absorption spectra at 80°K. Constant x = 0.05 and [P] is varied in samples (1) to (3).

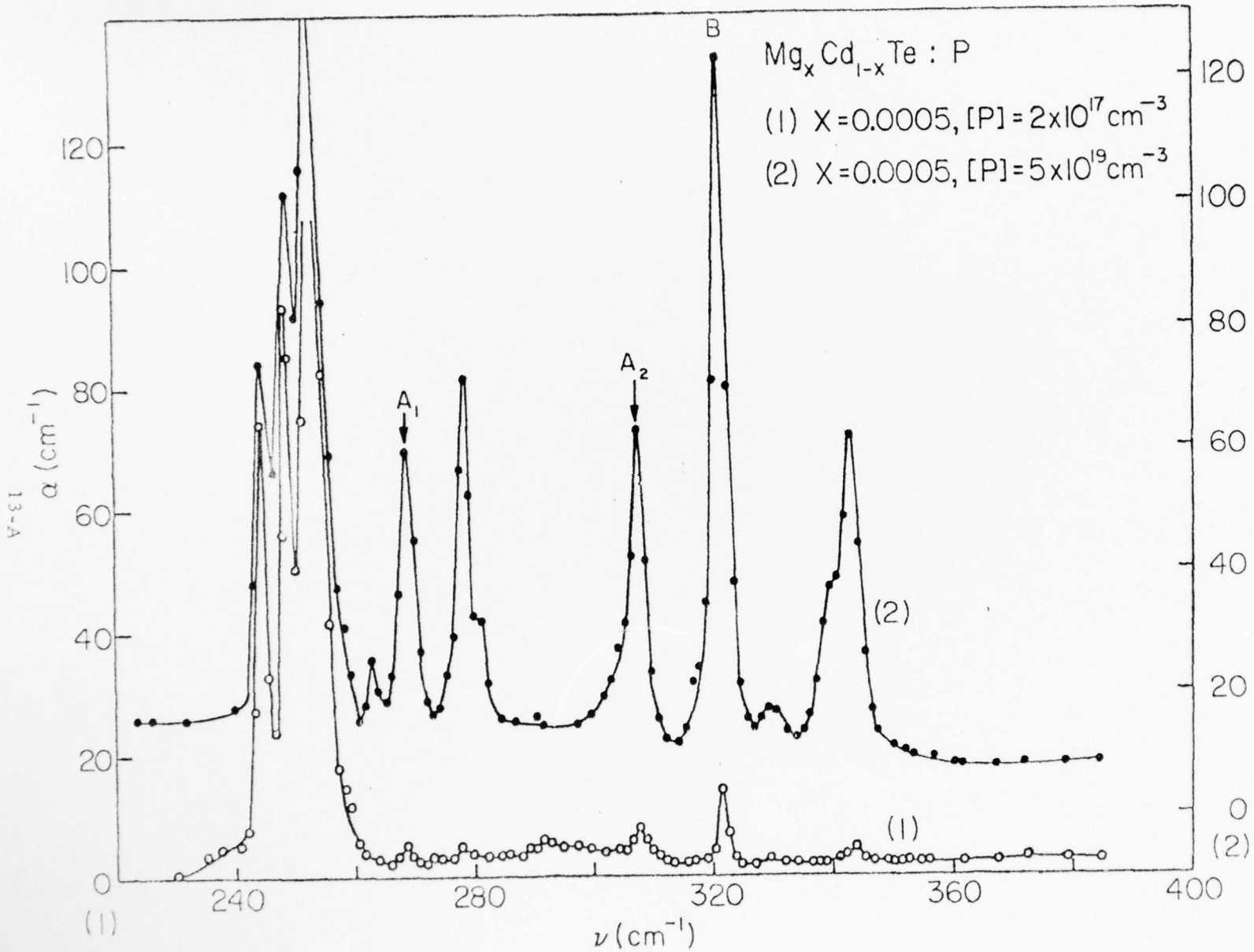
Figure 3 80°K abosrption spectra of $Mg_xCd_{1-x}Te$:P. x is varied keeping [P] $\approx 5 \times 10^{19} cm^{-3}$ in all (1) to (4) samples. The scale numbers correspond to the curve numbers.

Figure 4 80°K absorption spectra of $Mg_xCd_{1-x}Te$:P. [P] is varied keeping x = 0.0005 in samples (1) and (2). The scale numbers correspond to the curve numbers.


α, cm⁻¹
ν (cm⁻¹)
X = 0.2
(5)
X = 0.15
(4)
X = 0.05
(3)
X = 0.015
(2)
X = 0
(1)
A1
A2
B


(1) [P] ≈ 6 x 10^17 cm^-3
(2) [P] ≈ 1 x 10^18 cm^-3
(3) [P] ≈ 5 x 10^19 cm^-3
A1
A2
B
(1)
(2)
(3)
α (cm^-1)
ν (cm^-1)
0
10
20
30
40
50
60
70
80
90
100
260
280
300
320
340
360
380


$Mg_x Cd_{1-x} Te$: P(5×10^{19} cm^{-3})
(1) X = 0
(2) X = 0.0001
(3) X = 0.0005
(4) X = 0.05
B
A_1
A_2
α (cm^{-1})
ν (cm^{-1})
240
280
320
360
400


B
$Mg_x Cd_{1-x} Te$: P
(1) X=0.0005, [P]=2×10^{17} cm^{-3}
(2) X=0.0005, [P]=5×10^{19} cm^{-3}
A_1
A_2
(2)
(1)
α (cm^{-1})
ν (cm^{-1})
0
20
40
60
80
100
120
240
280
320
360
400
(1)
(2)

13-A

APPENDIX B

FREE CARRIER ABSORPTION OF n-TYPE ZnSe:Al*

B. V. Dutt, O. K. Kim and W. G. Spitzer

Departments of Physics and Materials Science

University of Southern California, Los Angeles, California 90007

ABSTRACT

Free carrier absorption measurements of ZnSe:Al annealed under Zn-rich conditions are reported. The absorption is nearly temperature independent, linear in carrier density and shows a ν^{-3} behavior. The experimental results are compared with calculations based on polar optical mode scattering. The agreement is reasonable except for the small temperature dependence observed in the experimental absorption. The conclusions are very similar to those reached previously for CdTe:Al.

* Work supported by the Defense Advanced Research Projects Agency under Contract No. F 19628-75-C-0162.

There has been considerable interest in recent years in the preparation and characterization of ZnSe. However, the present authors are not aware of any reports of free carrier absorption measurements of this material. The primary purpose of this communication is to give some measurements of the free carrier absorption of n-type ZnSe:Al.

The Al-doped ZnSe crystals were from Czochralski-grown ingots from the Eagle Picher Co. The Al concentration quoted here are those in the melt. The as-grown crystals are highly self-compensated and have no detectable free carrier absorption. The self-compensation mechanism in ZnSe is not well understood but it presumably involves the removal of the shallow donor level of Al, reported[1] to be 0.008 eV below the conduction band edge, by the formation of a $(Al_M\text{-}V_M)$ complex[2], where M refers to the metal sublattice site and V is a vacancy. Infrared absorption studies[3] of localized vibrational modes of ZnSe:Al showed more bands than can be accounted for by Al_{Zn} and $Al_{Zn}\text{-}V_{Zn}$ defects. The source of the additional bands in ZnSe:Al and other Zn-chalcogenides is not understood except that they appear to be related to the presence of the Al. On the other hand, CdTe:Al conforms to the simple picture and extra bands are not present.[4]

It is generally known that annealing ZnSe:Al in Zn-rich atmospheres suppresses the V_{Zn} concentration thereby reducing the self-compensation. For the free-carrier absorption measurements given here, a set of ZnSe crystals with different Al doping levels were an-

nealed in Zn-rich atmospheres. The samples were sealed in evacuated quartz ampoules with Zn shots and placed in two-zone furnace with the crystals at one end of the ampoule at 1160°K and the Zn-pool at the other end at ≤1160°K. The anneals were of 6 hours duration. For one sample an anneal was for 15 hours which showed no significant difference in free-carrier absorption from that of a similar sample annealed for 6 hours. After the anneals, the crystals were cooled to room temperature by dropping the ampoule into ethylene glycol.

The absorption measurements were performed on a Perkin-Elmer model 210 single beam grating monochromator. The carrier concentrations in the annealed samples were determined at 300°K and 80°K by using the Van der Pauw method to obtain $R_H = \frac{1}{n_e q}$. There was some initial difficulty in making good ohmic contacts. The best ones were obtained by following a method due to Aven[5]. After the optical measurements, the samples were etched in hot concentrated sodium hydroxide for 30-60 seconds and rinsed with hot distilled water. The desired contact pattern was scribed on the sample with a sharp-tipped In wire dipped in In-Hg amalgam. Extra In was added to the contacts by a soldering iron. The samples were then fired at 300°C in a stream of pure hydrogen for about a minute and quenched rapidly to room temperature. The Hall coefficient was then measured. As a check the absorption of sample #5 was remeasured after the contacting step and found to show no change. It is therefore assumed that the low temperature (300°C) cycling necessary for making the ohmic contacts has not altered the anneal-

produced condition of the samples.

The results of the absorption measurements are given by the data points in Fig. 1. The relevant information for the samples measured is given in Table I. Figure 2 shows a log-log plot of the absorption coefficient α, versus the carrier concentration, n_e, for $\nu = 2000\ cm^{-1}$ and $3000\ cm^{-1}$. From the absorption data in Figs. 1 and 2 it is apparent that, with the exception of sample #5, the spectral dependence is nearly the same and $\alpha \sim \nu^{-2.8}$ even though the samples have different Al concentrations. The magnitude of the absorption is nearly proportional to n_e and is independent of the Al concentration. These observations indicate that the lattice scattering absorption mechanism is the likely explanation for the measured absorption for samples #1 through 4. Sample #5 which has the highest carrier density and a large [Al] may have a contribution to the absorption from ionized impurity scattering which can have as large as a ν^{-4} dependence.

The curves A, a, B, b and C in Fig. 1 are theoretical estimates of $\alpha(\nu)$ calculated by using Jensen's theory [6, 7] for polar optical mode scattering. In this theory, the dependence of the absorption cross section, $\alpha(\nu)/n_e$, on temperature and frequency is contained in the term

$$\frac{1}{(h\nu)^3}\left[F_+(\nu, T)\, H_+(\nu) + F_-(\nu, T)\, H_-(\nu)\right],$$

where

$$F_{\pm}(\nu, T) = \sinh\left(\frac{h\nu}{2kT}\right)\left[2\sinh\left(\frac{h\nu_{LO}}{2kT}\right)\sinh\left(\frac{h\nu \pm h\nu_{LO}}{2kT}\right)\right]^{-1}$$

and $H_{\pm}$ are complex functions of $h\nu/kT$ and Δ_{so}/G, where Δ_{so} is the spin-orbit splitting energy and G is the bandgap energy. Jensen has shown that the expressions $H_{\pm}$ simplify considerably in the limits $\Delta_{so}/G \to 0$ and $\Delta_{so}/G \to \infty$. The $\alpha(\nu)$ curves A and B of Fig. 1 refer to $\Delta_{so}/G = 0$, $T = 300^{o}K$ and the room temperature n_e values for samples #1 and 5 respectively. The a and b are similar curves for $\Delta_{so}/G \to \infty$. The curve C refers to $\Delta_{so}/G = 0$, $T = 80^{o}K$ and for the $80^{o}K$ carrier density of sample #1, $n_e = 9.5 \times 10^{16} cm^{-3}$. In estimating these curves, the following values for parameters were used[8, 9]: $m_e^* = 0.17\ m_o$, $\varepsilon_\infty = 6.1$, $\varepsilon_o = 9.2$, $G(300^{o}K) = 2.58$ eV and $G(80^{o}K) = 2.74$ eV. With this choice of parameters, the calculated room temperature curves for a given n_e are both about a factor of two larger than the experimental absorption. Moreover, assuming a constant density the calculated $\alpha(300^{o}K)/\alpha(80^{o}K) \approx 1.9$ whereas the experimental ratio is only ≈ 1.2. The experimentally observed decrease in n_e of sample #1 between $300^{o}K$ and $80^{o}K$ makes the difference between the calculated and observed temperature dependence of α even larger. This difference is similar for all of the samples and is also very similar to that reported previously[4] for CdTe:Al.

TABLE I

Data of ZnSe: Al Samples

Sample No.	[Al](a) cm^{-3}	p_{Zn}, atm in anneal(b)	n_e, Carrier density, cm^{-3}		$\frac{\alpha(300^{\circ}K)}{n_e}$ at $\nu = 2000\ cm^{-1}$ cm^{-2}
			$300^{\circ}K$	$80^{\circ}K$	
1	3.8×10^{17}	0.7	1.6×10^{17}	9.5×10^{16}	2.6×10^{-17}
2	3.8×10^{18}	0.08	2.6×10^{17}	NM(c)	3.8×10^{-17}
3	3.8×10^{18}	0.7	5.7×10^{17}	2.9×10^{17}	2.9×10^{-17}
4	3.8×10^{19}	0.08	7.8×10^{17}	NM	4.6×10^{-17}
5	1.3×10^{19}	0.7	2.9×10^{18}	NM	2.7×10^{-17}

(a) Al concentration in the melt.

(b) Temperature of anneal = $1160^{\circ}K$; duration = 6 hours.

(c) NM: Not measured.

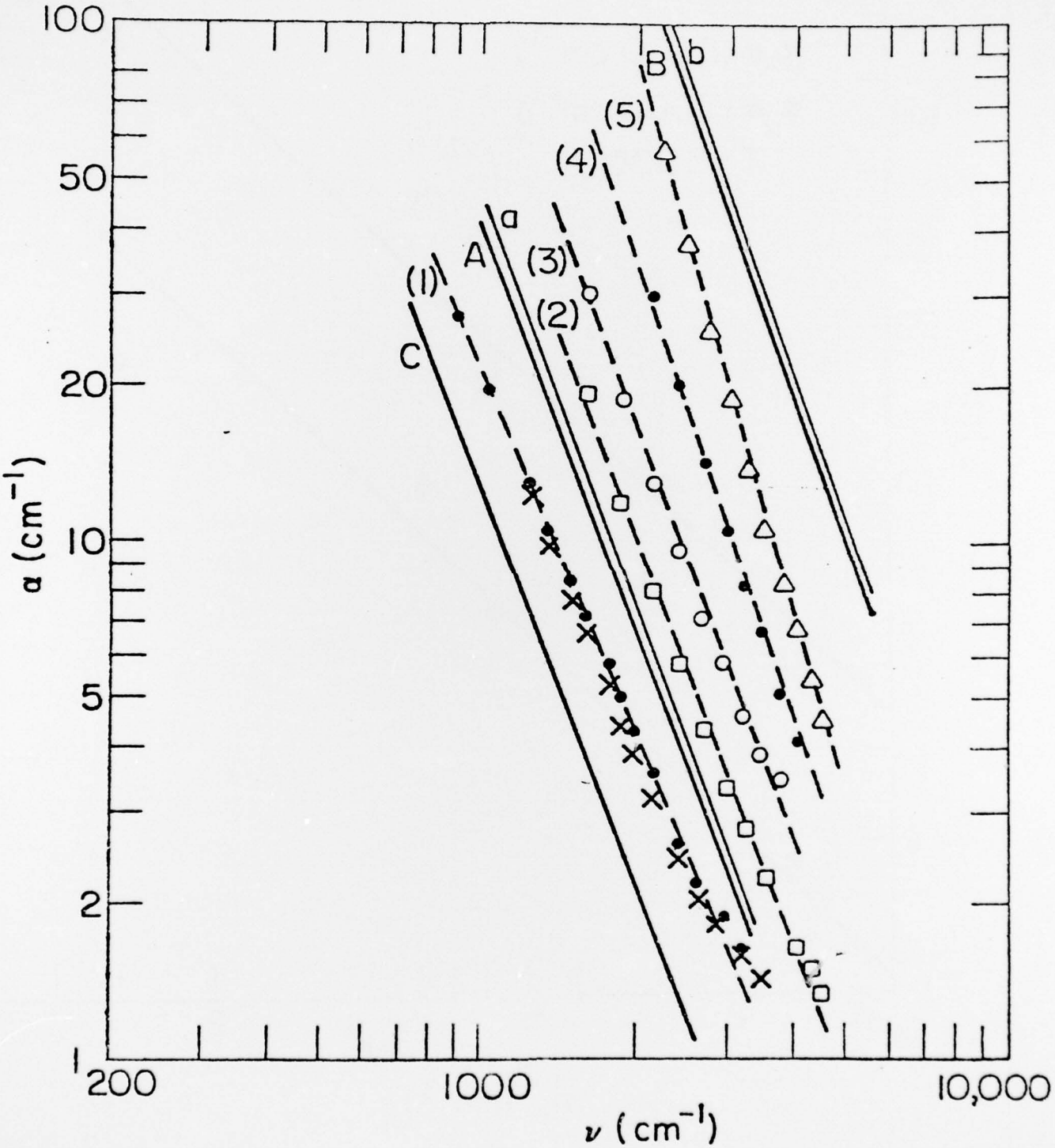
REFERENCES

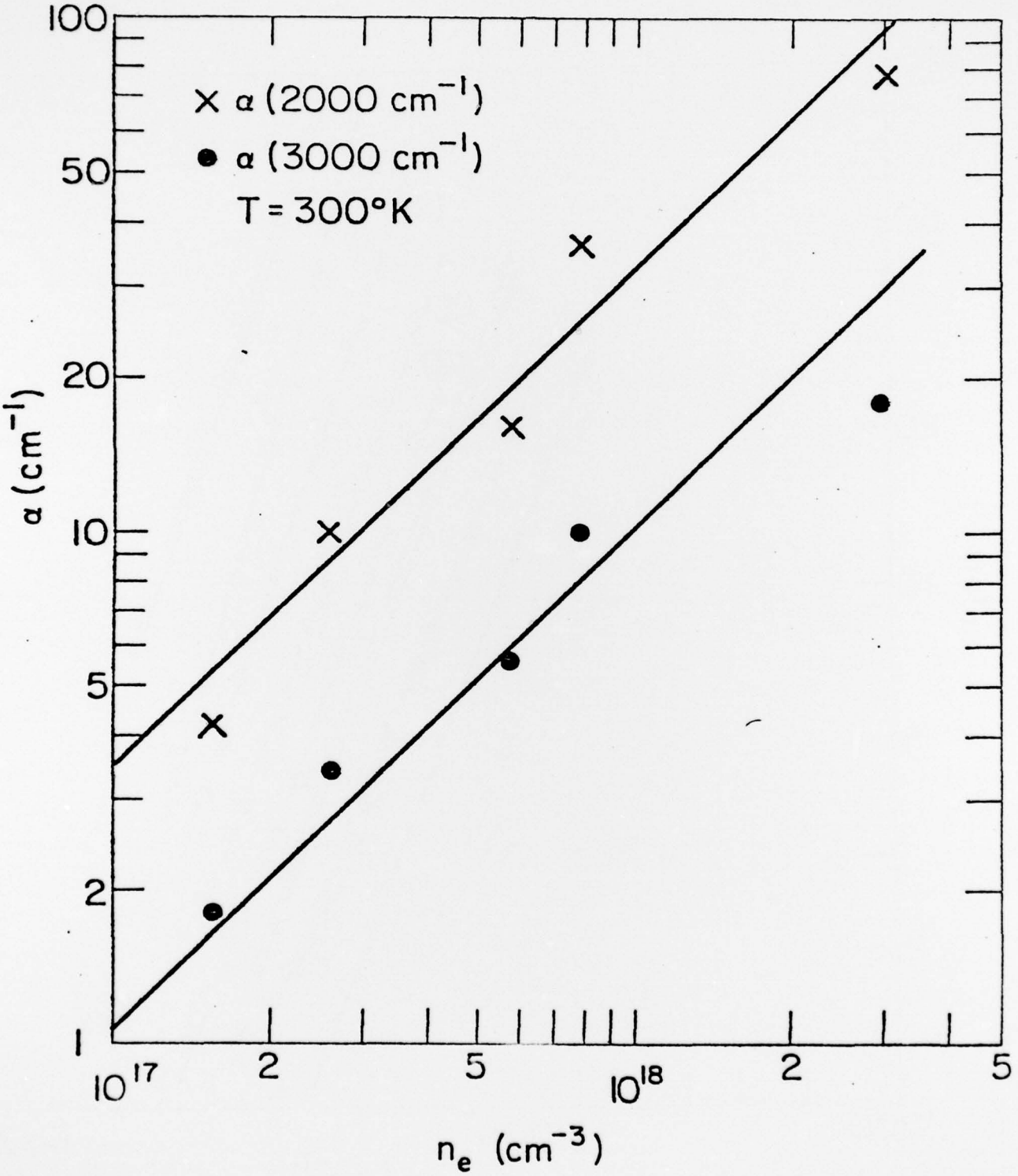
1. M. Aven and B. Segall, Phys. Rev. 130, 81 (1963).
2. M. Aven and J.S. Prener, Physics and Chemistry of II-VI Compounds, North-Holland Publishing Co., Amsterdam (1967).
3. A. Mitsuishi, A. Manabe, H. Yoshinaga, S. Ibuki and H. Komiya, Prog. Theor. Phys. 45 (Suppl.) 21 (1970); B. V. Dutt and W. G. Spitzer, J. Appl. Phys. 47, 573 (1976).
4. B. V. Dutt, M. Al-Delaimi and W. G. Spitzer, J. Appl. Phys. 47, 565 (1976).
5. M. Aven, private communication.
6. B. Jensen, J. Phys. Chem. Solids, 34, 2235 (1973).
7. B. Jensen, Ann. Phys. 80, 284 (1973).
8. M. Neuberger, II-VI Semiconducting Compounds Data Tables, Electronic Properties Information Center, Hughes Aircraft Co., Culver City, California, Rept. S-11, Oct. 1969. Available from the Defense Documentation Center (DDC), Alexandria, Virginia 22314.
9. J. I. Pankove, Optical Processes in Semiconductors, Prentice Hall, Inc., Englewood Cliffs, New Jersey (1971).

FIGURE CAPTIONS

Fig. 1 Absorption coefficient vs. frequency of Zn-annealed ZnSe:Al. The dashed lines connect the experimental data points. Numbers (1) - (5) refer to corresponding samples in Table I. The x-points are the 80°K data of sample 1. All other data are for 300°K. Solid lines give absorption calculated by using polar optical mode scattering. See text for details.

Fig. 2 Room temperature absorption coefficient vs. carrier density at $\nu = 2000\ cm^{-1}$ and $3000\ cm^{-1}$.


100
50
20
10
5
2
1
200
1000
10,000
α (cm⁻¹)
ν (cm⁻¹)
(1)
(2)
(3)
(4)
(5)
A
B
C
a
b


100
50
20
10
5
2
1
α (cm⁻¹)
× α (2000 cm⁻¹)
● α (3000 cm⁻¹)
T = 300°K
10¹⁷
2
5
10¹⁸
2
5
nₑ (cm⁻³)

METRIC SYSTEM

BASE UNITS:

Quantity	Unit	SI Symbol	Formula
length	metre	m	...
mass	kilogram	kg	...
time	second	s	...
electric current	ampere	A	...
thermodynamic temperature	kelvin	K	...
amount of substance	mole	mol	...
luminous intensity	candela	cd	...

SUPPLEMENTARY UNITS:

plane angle	radian	rad	...
solid angle	steradian	sr	...

DERIVED UNITS:

Acceleration	metre per second squared	...	m/s
activity (of a radioactive source)	disintegration per second	...	(disintegration)/s
angular acceleration	radian per second squared	...	rad/s
angular velocity	radian per second	...	rad/s
area	square metre	...	m
density	kilogram per cubic metre	...	kg/m
electric capacitance	farad	F	A-s/V
electrical conductance	siemens	S	A/V
electric field strength	volt per metre	...	V/m
electric inductance	henry	H	V-s/A
electric potential difference	volt	V	W/A
electric resistance	ohm		V/A
electromotive force	volt	V	W/A
energy	joule	J	N-m
entropy	joule per kelvin	...	J/K
force	newton	N	kg-m/s
frequency	hertz	Hz	(cycle)/s
illuminance	lux	lx	lm/m
luminance	candela per square metre	...	cd/m
luminous flux	lumen	lm	cd-sr
magnetic field strength	ampere per metre	...	A/m
magnetic flux	weber	Wb	V-s
magnetic flux density	tesla	T	Wb/m
magnetomotive force	ampere	A	...
power	watt	W	J/s
pressure	pascal	Pa	N/m
quantity of electricity	coulomb	C	A-s
quantity of heat	joule	J	N-m
radiant intensity	watt per steradian	...	W/sr
specific heat	joule per kilogram-kelvin	...	J/kg-K
stress	pascal	Pa	N/m
thermal conductivity	watt per metre-kelvin	...	W/m-K
velocity	metre per second	...	m/s
viscosity, dynamic	pascal-second	...	Pa-s
viscosity, kinematic	square metre per second	...	m/s
voltage	volt	V	W/A
volume	cubic metre	...	m
wavenumber	reciprocal metre	...	(wave)/m
work	joule	J	N-m

SI PREFIXES:

Multiplication Factors	Prefix	SI Symbol
1 000 000 000 000 = 10^{12}	tera	T
1 000 000 000 = 10^{9}	giga	G
1 000 000 = 10^{6}	mega	M
1 000 = 10^{3}	kilo	k
100 = 10^{2}	hecto*	h
10 = 10^{1}	deka*	da
0.1 = 10^{-1}	deci*	d
0.01 = 10^{-2}	centi*	c
0.001 = 10^{-3}	milli	m
0.000 001 = 10^{-6}	micro	μ
0.000 000 001 = 10^{-9}	nano	n
0.000 000 000 001 = 10^{-12}	pico	p
0.000 000 000 000 001 = 10^{-15}	femto	f
0.000 000 000 000 000 001 = 10^{-18}	atto	a

* To be avoided where possible

MISSION
of
Rome Air Development Center

RADC plans and conducts research, exploratory and advanced development programs in command, control, and communications (C^3) activities, and in the C^3 areas of information sciences and intelligence. The principal technical mission areas are communications, electromagnetic guidance and control, surveillance of ground and aerospace objects, intelligence data collection and handling, information system technology, ionospheric propagation, solid state sciences, microwave physics and electronic reliability, maintainability and compatibility.

Printed by
United States Air Force
Hanscom AFB, Mass. 01731